TAMPEREEN TEKNILLINEN YLIOPISTO
TAMPERE UNIVERSITY OF TECHNOLOGY

AJITH ADHUR KUTTY

CARBON NANOTUBE LOADED PASSIVE UHF RFID SENSOR TAG WITH BUILT-IN REFERENCE FOR WIRELESS GAS SENSING

Master of Science thesis

Examiners: Prof. Leena Ukkonen,
Prof. Lauri Sydänheimo
Examiners and topic approved by the
Faculty Council of the Faculty of
Computing and Electrical Engineering
on 13th January 2016

ABSTRACT

AJITH ADHUR KUTTY: Carbon Nanotube Loaded Passive UHF RFID Sensor Tag with Built-in Reference for Wireless Gas Sensing
Tampere University of Technology
Master of Science thesis, 67 pages, 0 Appendix pages
February 2016
Master's Degree Programme in Electrical Engineering
Major: Wireless Communication
Examiner: Prof. Leena Ukkonen and Prof. Lauri Sydänheimo
Keywords: Carbon Nanotubes, Gas detectors, Inkjet-Printing, Passive microwave remote sensing, RFID Tags.

Radio Frequency IDentification (RFID) technology, which uses communication by means of reflected power [49], is used for the wireless identification of objects [65]. Individual objects are identified by the RFID tag placed on them. An RFID tag consists of a microchip and an antenna. An RFID reader transmits radio frequency (RF) waves to identify the tagged objects. It transmits identification information, which is stored in its memory, through back scattered radio waves to the RFID reader. Passive RFID tags harvests RF energy from the reader device to power its microchip, enabling battery free operation.

Passive wireless sensors based on UHF RFID technology are a promising prospect in the realm of ubiquitous sensing and Internet of Things (IoT) [36],[19]. The sensing principles and methods used depend on the variation of the tag antenna gain, the impedance match between the tag antenna and the RFID chip, or both, with respect to the sensed parameter [36]. The RFID reader uses back scattered RF signal properties to perform sensing. Usually, threshold power, the power at which an RFID tag harvests enough power to turn itself ON, or back scattered signal power, is used for sensing measurements. These measurements depend heavily on the environment, where the tag is placed, and the distance at which it is measured by a reader. This poses severe restrictions in sensing measurements. To maintain sensor accuracy, precise calibration of the measurement setup is required [60]. Any disturbance in the measurement setup or the RF propagation environment affect the sensor measurement.

This thesis presents a novel architecture of inkjet-printed passive UHF RFID based

sensor tag that allows a reference measurement and sensing measurement for wireless gas sensing [1]. In this work, an RFID tag is made with Silver (Ag) ink, and is loaded with carbon nanotube (CNT) ink for sensing purpose. Carbon nanotubes (CNT) have a property that it modifies its conductivity in the presence of certain gases [55]. This property is exploited for sensing (CO_2) gas. A switch, used in the sensor tag's structure, provides two modes of operation. They are, sensor on (SON) or sensing mode operation, and sensor off (SOFF) or reference mode operation. In SON mode, the sensor tag modifies its backscatter properties in the presence of gas. In SOFF mode, the realized gain of the sensor tag remains constant in the presence of gas, which provides a reference measurement. The difference in threshold power, between SON mode and SOFF mode is used as the sensing parameter. This sensing paradigm allows sensor measurements that do not depend on the RF propagation conditions, or the distance of the reader. The fabricated sensor tags, when exposed to CO_2, show a threshold power variation of up to 2dB, with a read range of about 4m at 915MHz. This means, threshold power difference between SON and SOFF mode provides unambiguous detection of CO_2 at all measurement conditions.

Study and measurements done in this work prove the feasibility of gas detection by placing CNT very close to the tag, instead of, on the tag. More importantly, the concept of using a switch in the sensor tag to provide reference measurement is proven. Several possibilities exist in the realization of the switch including, but not limited to, incorporating the switch within the RFID chip. These ideas will be explored in future work.

PREFACE

This thesis was made in partial fulfillment of the requirement for the Master of Science Degree in Electrical Engineering, at the Department of Electronics and Communications Engineering, Tampere University of Technology, Finland. All the research and investigations covered under this work are done at Wireless Identification and Sensing Systems (WISE) research group at Tampere University of Technology, under the supervision of Prof. Leena Ukkonen and Prof. Lauri Sydäheimo.

I would like to express gratitude to my esteemed supervisors for the opportunity to be part of WISE and providing a supportive and stimulating environment to complete this work. It was a pleasure to work with Muhammad Rizwan and Johanna Virkki, while learning inkjet printing. I thank them for their support. I thankfully remember all guidance from Toni Björninen, Postdoctoral Researcher. I like to thank also Mitra Akbari, for all the information and advice on materials that made this work possible. Let me not forget, all other members of WISE for encouragement and support.

Several courses on Electromagnetic Theory and Antennas conducted by Lecturer Jari Kangas enabled me to perform this work. I thank him for all the learning and guidance through all his courses. I would like to acknowledge Guillaume Krosnicki of Poly-ink for his valuable support, which enabled printing CNT ink. I take this opportunity to thank Lassi Sukki, from Automation Science and Engineering department of TUT, for his support with oxygen plasma treatment.

I take this opportunity to thank my parents who have been an inspiration in various ways. My deepest gratitude goes to my wife for her unending love, and support, that helped me pursue this work. I apologize, to my kids, for sacrificing the times that I could have spent with them.

Tampere,
24/02/2016

Ajith Adhur Kutty

TABLE OF CONTENTS

LIST OF FIGURES

LIST OF TABLES

LIST OF ABBREVIATIONS AND SYMBOLS

Ag	Silver
CNT	Carbon NanoTube.
DC	Direct Current.
DoD	Drop on Demand.
DPI	Dots Per Inch.
EIRP	Equivalent Isotropic Radiated Power.
EU	European Union.
GIMP	Gnu Image Manipulation Program.
JPEG	Joint Photographic Experts Group.
MSDS	Material Safety Data Sheet.
MWCNT	Multi-Walled Carbon Nanotube.
NEC	Numeric Electromagnetic Code.
PEDOT:PSS	Poly(3,4-ethylenedioxythiophene) Polystyrene Sulfonate
PTFE	Polytetrafluoroehtylene.
PVDF	Polyvinylidene Fluoride.
RF	Radio Frequency.
RFID	Radio Frequency Identification.
SWCNT	Single-Walled Carbon Nanotube.
sccm	Standard Cubic Centimeter Per Minute.
UHF	Ultra High Frequency.
WISE	Wireless Identification and Sensing Systems.

1. INTRODUCTION

We as human always strive to gather better and deeper understanding of our environment, for the improvement or safety of our lives. Ubiquitious sensing of our environment using wireless sensor networks is slowly becoming a practical reality. It is enabled by the development of energy efficient, and miniature sensors in recent years. Advancements in wireless communication and computing systems over the past few decades enabled us to interconnect such miniature sensor modules, creating ubiquitious wireless sensor networks. Connectivity of such wireless sensor networks to the internet give the capability to collect and store large amount of data regading our environment. Intelligent signal and data processing algorithms along with ubiquitious wireless sensor networks help us to create intelligent environments that can improve human productivity and quality of life. Developing environmental sensing and monitoring technologies is beneficial for industries that may cause severe contamination due to the handling of toxic chemicals.

Radio Frequency IDentification (RFID) based passive wireless sensors are ideal candidates for energy efficient, low maintenance, and miniature sensors [30]. RFID is a technology created for wireless identification or tagging of all the objects in this world [15]. RFID offers an energy efficient and maintenance free platform for creating wireless sensors. Integrating independent sensors into the RFID chip is one way of achieving it. Another attractive approach is to make the properties of the antenna or the impedance match between the chip and antenna to vary depending on a sensing parameter [29]. Recent development of nanotechnology has created materials that can be used with an RFID tag to create versatile sensors. The extremely high surface-to-volume ratio and hollow structure of nanomaterials is ideal for gas molecules' adsorption and storage. Therefore, gas sensors based on nanomaterials, such as carbon nanotubes (CNTs), nano-wires, nano-fibers, and nano-particles, have been investigated widely [63].

This thesis proposes and validates the functioning of a novel, passive UHF RFID

based, wireless sensor tag for the detection of CO_2 gas in the environment. The key development in this work is that it allows a reference measurement, which when used relative to the sensing measurement helps accurate detection of gas [1]. This report initially covers the theoretical background in chapter 2 which is required to appreciate the work involved. Chapter 3 covers the motivation, materials, design, simulation, sensing methods, fabrication method and measurements used for this work. This chapter also provides a brief account of inkjet-printing and an extensive coverage of some of the challenges involved in inkjet-printing. Measurement results are analyzed and discussed in chapter 4 and the work is concluded with ideas for future work in chapter 5.

2. THEORETICAL BACKGROUND

This chapter glances upon some of the theoretical aspects involved in the conception, design, measurement and validation of the sensor tag proposed in this thesis. This chapter intends to help refreshing some of the relevant aspects of electromagnetic theory, antenna theory and design, and microwave engineering to someone who has prior knowledge of them. This chapter is by no means an exhaustive coverage of all theoretical aspects of this work. Its rather a humbling experience to give snapshots of what is already extensively covered in excellent books, such as, [6], [50], [20], and [41]. A brief introduction to RFID technology and subsequently passive UHF RFID based sensor tags are given in later sections of this chapter. These brief introductions takes us closer to the topic of the thesis and include pointers to scientific literature that gives a wider coverage regarding specific details.

2.1 Maxwell's Equations

James Clark Maxwell set out twenty equations, which Oliver Heaviside later condensed to four equations, that forms the foundation of electromagnetic theory, electromagnetic wave propagation and antenna theory. Maxwell's equations which is a collection of Faraday's law of induction, Ampere's law, Gauss's law and Gauss's law of magnetism are given below in point form (differential) and integral form [20].

$$\nabla \times \vec{\mathbf{E}} = -\frac{\partial \vec{\mathbf{B}}}{\partial t} \quad \Rightarrow \quad \oint_c \vec{\mathbf{E}} \cdot \vec{dl} = -\int_s \frac{\partial \vec{\mathbf{B}}}{\partial t} \cdot \vec{ds} \tag{2.1}$$

$$\nabla \times \vec{\mathbf{H}} = \vec{\mathbf{J}} + \frac{\partial \vec{\mathbf{D}}}{\partial t} \quad \Rightarrow \quad \oint_c \vec{\mathbf{H}} \cdot \vec{dl} = \int_s \vec{\mathbf{J}} \cdot \vec{ds} + \int_s \frac{\partial \vec{\mathbf{D}}}{\partial t} \cdot \vec{ds} \tag{2.2}$$

$$\nabla \cdot \vec{\mathbf{D}} = \rho_v \quad \Rightarrow \quad \oint_s \vec{\mathbf{D}} \cdot \vec{ds} = \int_v \rho_v dv \tag{2.3}$$

$$\nabla \cdot \vec{\mathbf{B}} = 0 \quad \Rightarrow \quad \oint_s \vec{\mathbf{B}} \cdot \vec{ds} = 0 \tag{2.4}$$

where,
$\vec{\mathbf{E}}$ = electric field intensity (vector), in $\mathrm{V\,m^{-1}}$
$\vec{\mathbf{H}}$ = magnetic field intensity (vector), in $\mathrm{A\,m^{-1}}$
$\vec{\mathbf{D}}$ = electric flux intensity (vector), in $\mathrm{C\,m^{-2}}$
$\vec{\mathbf{B}}$ = magnetic flux intensity (vector), in $\mathrm{Wb\,m^{-2}}$
$\vec{\mathbf{J}}$ = volume current density (vector), in $\mathrm{A\,m^{-2}}$
ρ_v = free volume charge density (scalar), in $\mathrm{C^3\,m^{-1}}$

and ∇ is the Del operator or vector differential operator.

The ***constitutive equations***, define the relationships between field quantities in Maxwell's equations. Given below are the constitutive equations for a linear, homogeneous, and isotropic medium.

$$\vec{\mathbf{D}} = \epsilon\vec{\mathbf{E}} \tag{2.5}$$
$$\vec{\mathbf{J}} = \sigma\vec{\mathbf{E}} \tag{2.6}$$
$$\vec{\mathbf{B}} = \mu\vec{\mathbf{H}} \tag{2.7}$$

where,
ϵ = permittivity (scalar), in $\mathrm{F\,m^{-1}}$
μ = permeability (scalar), in $\mathrm{H\,m^{-1}}$
σ = conductivity (scalar), in $\mathrm{S\,m^{-1}}$

Equation 2.6 is the well known *Ohm's law*.

Boundary conditions are required to obtain the full solution of electromagnetic fields from solving the partial differential or integral equations. The boundary conditions are expressed below in its vector form.

$$\vec{\mathbf{a}}_n \times (\vec{\mathbf{E}}_1 - \vec{\mathbf{E}}_2) = 0 \tag{2.8}$$
$$\vec{\mathbf{a}}_n \times (\vec{\mathbf{H}}_1 - \vec{\mathbf{H}}_2) = \vec{\mathbf{J}}_s \tag{2.9}$$
$$\vec{\mathbf{a}}_n \cdot (\vec{\mathbf{B}}_1 - \vec{\mathbf{B}}_2) = 0 \tag{2.10}$$
$$\vec{\mathbf{a}}_n \cdot (\vec{\mathbf{D}}_1 - \vec{\mathbf{D}}_2) = \rho_s \tag{2.11}$$
$$\vec{\mathbf{a}}_n \cdot (\vec{\mathbf{J}}_1 - \vec{\mathbf{J}}_2) = 0 \tag{2.12}$$

$$\vec{\mathbf{a}}_n \times \left[\frac{\vec{\mathbf{J}}_1}{\sigma_1} - \frac{\vec{\mathbf{J}}_2}{\sigma_2}\right] = 0 \tag{2.13}$$

The subscripts 1 and 2 are used to refer to the quantities in medium 1 and 2 respectively. $\vec{\mathbf{a}}_n$ is the unit vector at the interface normal to the boundary and points into medium 1.

Solution of Maxwell's equations with the boundary conditions leads us to electromagnetic wave propagation in free space. It proves electromagnetic wave propagation with the velocity of speed of light. It provides solutions to electromagnetic fields setup by current distribution in a radiating element like an antenna.

2.2 Antennas

Antennas are terminals used to carry the electrical signals through empty space. While a transmission line would confine the electromagnetic wave that it carries to the region, near, or inside it, an antenna would radiate electromagnetic waves to reach large distances. The IEEE defines an antenna as "that part of a transmitting or receiving system that is designed to radiate or to receive electromagnetic waves." [Sec. H.2: "IEEE Standard Definition of Terms for Antenna"] An antenna can be viewed as a *transducer* that converts a guided (or bound) wave on a transmission line to a free-space electromagnetic wave (for the transmitting case) or vice versa (for the receiving case) [50].

There are several different types of antennas. They can be broadly classified into four categories, Resonant antennas (eg. Half-wave dipole, Microstrip patch), Broadband Antennas (eg. spiral, log-periodic dipole array), Aperture antennas (eg. Horn, Reflector), and Electrically small antennas (eg. short dipole). The resonant half-wave dipole antenna is significant to this work and is briefly covered later. First some of the fundamental antenna parameters are explored in the next section.

2.2.1 Antenna Parameters

Some of the antenna parameters, that is relevant to this thesis, describing the performance of the antenna are defined in this section.

2.2.1.1 Radiation Pattern

At a distance far away, larger than the size of the antenna and the wavelength, the nature of electromagnetic fields is independent of distance. Thus we are able to obtain far field patterns which are independent of distance.

An *antenna radiation pattern* or *antenna pattern* is defined as "a mathematical function or a graphical representation of the radiation properties of the antenna as a function of space coordinates. In most cases, the radiation pattern is determined in the far field region and is represented as a function of the directional coordinates. Radiation properties include power flux density, radiation intensity, field strength, directivity, phase or polarization. [6]". The radiation pattern of a dipole antenna is shown in figure 2.1.

Radiation intensity in a given direction is defined as "the power radiated from an antenna per unit solid angle. [6]" It can be expressed as,

$$U = r^2 W_{rad} \tag{2.14}$$

where U is the radiation intensity (W/unitsolidangle) and W_{rad} is the radiation density ($\mathrm{W\,m^{-1}}$)

2.2.1.2 Directivity and Gain

Directivity of an antenna is defined as "the ratio of the radiation intensity in a given direction from the antenna to the radiation intensity averaged over all directions. The average radiation intensity is equal to the total power radiated by the antenna divided by 4π. If the direction is not specified, the direction of maximum radiation intensity is applied. [6]"

$$D = \frac{U_m}{U_{ave}} = \frac{4\pi U_m}{P_{rad}} \tag{2.15}$$

Directivity of an antenna is solely determined by the radiation pattern of an antenna. Gain of the antenna is needed to know how efficiently the antenna transforms available power at its terminals into radiated power.

Gain of an antenna (in a given direction) is defined as "the ratio of the intensity,

in a given direction, to the radiation intensity that would be obtained if the power accepted by the antenna were radiated isotropically. The radiation intensity corresponding to the isotropically radiated power is equal to the power accepted by the antenna divided by 4π. [6]".

$$G = \frac{4\pi U_m}{P_{in}} \tag{2.16}$$

2.2.1.3 Antenna Impedance

The antenna is an interface between wave phenomena on and beyond the antenna to the connecting circuit hardware. The connecting circuit would need the input impedance at antenna terminals to characterize the interface. This input impedance (or antenna impedance) is defined as "the impedance presented by an antenna at its terminals or the ratio of the voltage to current at a pair of terminals or the ratio of the appropriate components of the electric to magnetic fields at a point. [6]"

Antenna impedance is composed of real and imaginary parts.

$$Z_A = R_A + jX_A \tag{2.17}$$

Here the resistive part consists of two components,

$$R_A = R_r + R_o \tag{2.18}$$

where R_r is the radiation resistance, the power dissipated in which represents the radiated power of the antenna and R_o is the ohmic resistance, the power dissipated in which represents the ohmic losses in the antenna structure.

The input impedance of the antenna will be affected by other antennas or objects that are nearby [50], but typically antennas are studied or simulated while keeping in free space.

2.2.1.4 Radiation Efficiency

The radiation efficiency of an antenna is the ratio of radiated power to the net power accepted by the antenna:

$$e_r = \frac{P}{P_{in}} = \frac{P}{P + P_o}, \tag{2.19}$$

where P is radiated power, P_o is the power dissipated in ohmic losses on the antenna and P_{in} is the power accepted by the antenna. It can be shown that,

$$e_r = \frac{R_r}{R_r + R_o}. \tag{2.20}$$

This shows that higher ohmic losses in the antenna results in poorer radiation efficiency.

When efficiency is considered with the net power fed to the antenna terminals, then it results in the total efficiency of the antenna. Here we consider the mismatch losses between the antenna and the feeding transmission line.

2.2.1.5 Polarization

Polarization of an antenna is defined as the polarization of the wave transmitted (radiated) by the antenna in the direction of the maximum gain.

Polarization of a radiated wave is defined as that property of an electromagnetic wave describing the time-varying direction and relative magnitude of the electric-field vector; specifically, the figure traced as a function of time by the extremity of the vector at a fixed location in space, and the sense in which it is traced, as observed along the direction of propagation. Different types of polarization include linear polarization, left or right circular polarization, and elliptical polarization.

When the polarization of the receiving antenna is not the same as the polarization of the incident wave, then the amount of power extracted by the antenna from the incoming signal will not be the maximum because of the polarization loss. *Polarization efficiency*, or in other words, *polarization mismatch factor* or *loss factor*, is defined as the ratio of the power received by an antenna from a given plane wave of the same power flux density and direction of propagation, whose state of polarization has been adjusted for a maximum received power [6].

2.2.2 Half-wave Dipole Antenna

The antenna design used for this thesis work is based on a half-wave dipole antenna. A half-wave dipole antenna is realized with a straight wire of length equal to half of wavelength and fed in the center. The amplitude distribution of the linear current fed to the dipole is sinusoidal in nature with a maximum at the center. The electric and magnetic field components of a half-wavelength dipole can be obtained using this sinusoidal current distribution and solving Maxwell's equations. When the dipole is kept vertical along the z-axis with feed point at the origin, the field components are found to be,

$$E_\theta \simeq j\eta \frac{I_0 e^{-jkr}}{2\pi r}\left[\frac{cos\left(\frac{\pi}{2}cos\theta\right)}{sin\theta}\right], \tag{2.21}$$

$$H_\phi \simeq \ j\frac{I_0 e^{-jkr}}{2\pi r}\left[\frac{cos\left(\frac{\pi}{2}cos\theta\right)}{sin\theta}\right], \tag{2.22}$$

where θ and ϕ indicates the vector components in spherical coordinate system, k is the complex wave propagation constant, η is the characteristic impedance of the medium and r is the radial distance from origin. These field components results in the radiation pattern shown in figure 2.1.

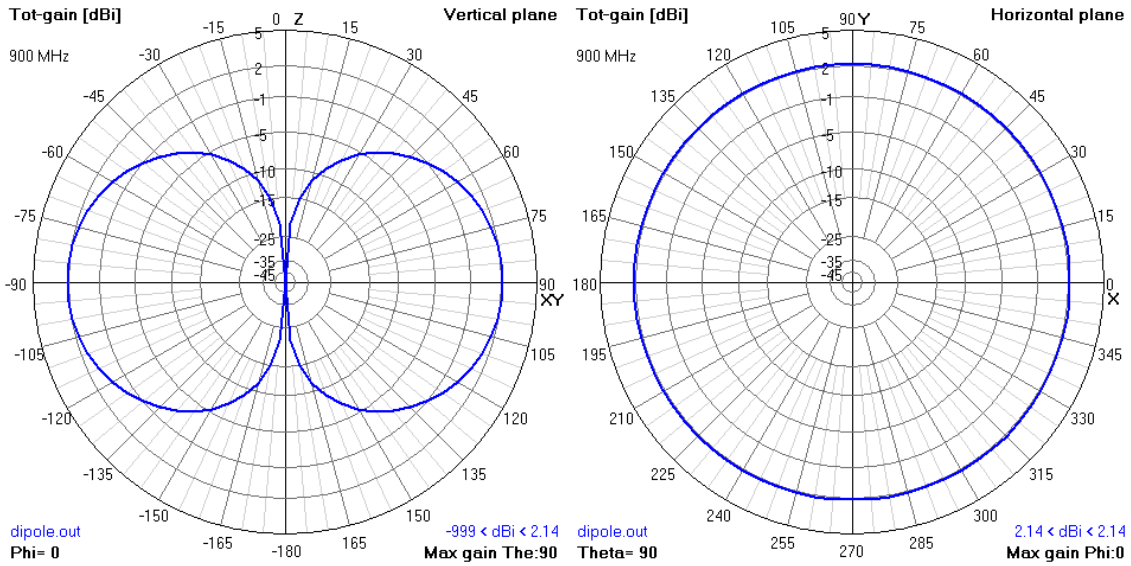

(a) Radiation pattern in vertical plane. **(b)** Radiation pattern in horizontal plane.

Figure 2.1 *Radiation pattern, obtained from 4NEC2 simulation, of a half wave dipole antenna kept vertically along the z-axis.*

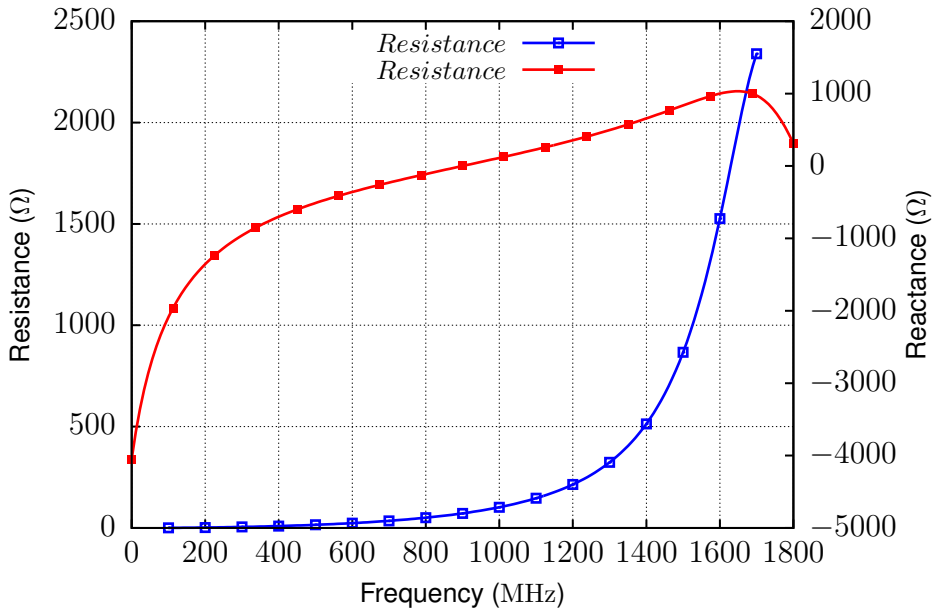

Figure 2.2 *Resistive and reactive part of the impedance of a half wave dipole antenna with resonant frequency* 900 MHz. *Obtained from 4NEC2 simulation results.*

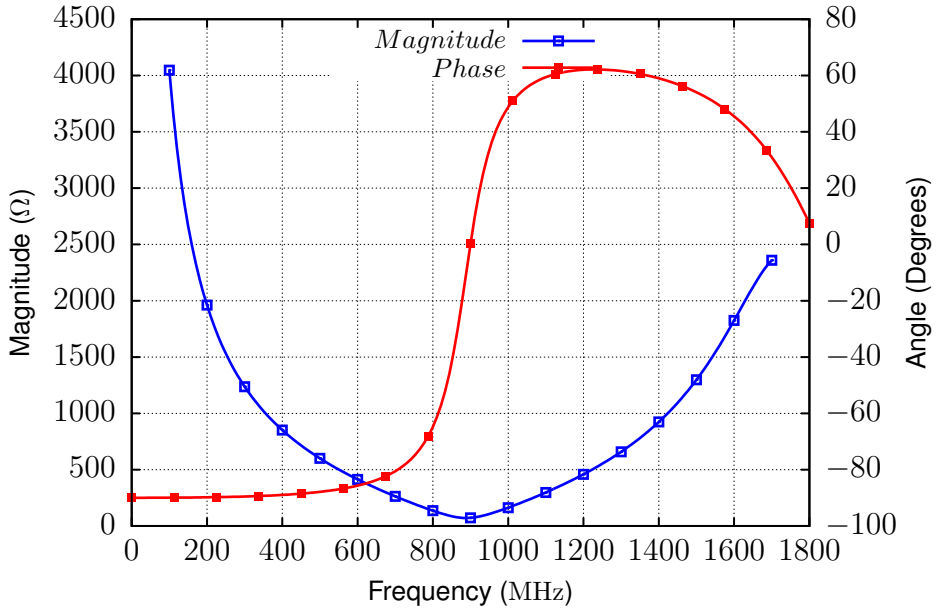

Figure 2.3 *Magnitude and phase of input impedance of a half wave dipole antenna with resonant frequency* 900 MHz. *Obtained from 4NEC2 simulation results.*

The input impedance of an infinitely thin dipole of exactly one-half wavelength is $Z_A = 73 + j42.5\Omega$ [50]. The nature of variation of input impedance of a half-wave dipole with a resonant frequency of 900 MHz is shown in figure 2.2 and figure 2.3.

The figure 2.3 shows the resonant behavior of the antenna with resonant frequency close to 900 MHz. Also these figures show that a dipole of shorter lengths will have input impedance that is capacitive in nature and a dipole of longer length will have inductive input impedance at the same frequency.

The maximum directivity of the half-wavelength dipole can be shown as,

$$D = \frac{4\pi U_m}{P_{rad}} = 1.64 = 2.15\,\text{dBi} \tag{2.23}$$

2.3 Effective Isotropically Radiated Power

Effective Isotropically Radiated Power or EIRP, is the amount of power emitted from an isotropic antenna to obtain the same power density in the direction of the antenna pattern peak with a specific gain. EIRP in other words is the gain of the transmitting antenna multiplied by the net power accepted by the antenna for transmission. i.e.,

$$EIRP = P_t.G_t \tag{2.24}$$

where P_t is the power accepted by the antenna and G_t is the gain of the transmitting antenna.

2.4 Conjugate Impedance Matching

A power source having source impedance, Z_G, delivers maximum power to load, Z_L, when the load impedance is equal to the complex conjugate of load impedance. i.e.,

$$Z_L = Z_G^* \tag{2.25}$$

$$\implies R_L + jX_L = R_G - jX_G. \tag{2.26}$$

This condition is known as conjugate matching, and it results in maximum power transfer to the load from a fixed generator impedance. The maximum power delivered being [41],

$$P = \frac{1}{2}|V_G|^2 \frac{1}{4R_G}, \tag{2.27}$$

where V_G is the voltage of the source.

When there is a mismatch between the source and load impedance, only a fraction

of the maximum power gets transferred from the source to the load. This fraction is expressed by the power transmission coefficient expressed as [50],

$$\tau = \frac{4R_A R_L}{(R_A + R_L)^2 + (X_A + X_L)^2}. \tag{2.28}$$

The power transmission coefficient is also called the impedance mismatch factor.

2.5 Realized Gain

Gain of the antenna defined in section 2.2.1, is based on the power that is accepted by the antenna terminals. If there is an impedance mismatch between the source and the antenna, then only a fraction of the power fed to the antenna is accepted by the antenna. Gain of the antenna defined by taking into account the mismatch losses is called the absolute gain or realized gain of the antenna. Realized gain can be expressed as,

$$G_r = \tau.G, \tag{2.29}$$

where τ is the power transmission coefficient and G is the gain of the antenna.

2.6 Friis Transmission Equation

Friis transmission equation specifies the power transfer in a communication link involving a transmitting and receiving antenna, expressed in the simplest form as [50],

$$P_r = P_t \frac{G_t G_r \lambda^2}{(4\pi R)^2}, \tag{2.30}$$

where P_r is the power received by the receiving antenna, P_t is the power transmitted by the transmitting antenna, G_t is the gain of the transmitting antenna, G_r is the gain of the receiving antenna, λ is the wavelength used for transmission and R is the distance of separation between the receiving and transmitting antennas.

This expression shall be modified, expressing the actual power fed to the transmitting antenna and the actual power that is delivered to the receiver by the receiving antenna, by accounting the impedance mismatch loss at the antenna terminals. Then the gain terms in equation 2.30 need to be modified as the realized gain values. Also there can be polarization mismatch between the receiving and transmitting antennas, due to their misalignment with each other. Hence a modified expression for

Friis transmission equation can be given as,

$$P_r = \left(\frac{\lambda}{4\pi R}\right)^2 . G_{rT} . G_{rR} . \eta_P . P_t, \tag{2.31}$$

where G_{rT} is the realized gain of transmitting antenna, G_{rR} is the realized gain of receiving antenna and η_P is the polarization efficiency.

2.7 Skin Depth

Current flow due to alternating current doesn't get uniformly distributed across the cross section of the conductor that carries it. Depending on the frequency of the alternating current the current flow is restricted to the regions close to the outer surfaces of the conductor. The concentration of the current in a thin layer next to the surface of the conductor results in an increase in its resistance. This phenomenon is called the *skin effect* [20].

Skin depth, or characteristic depth of penetration, is the depth of penetration of the electromagnetic field or the current inside the surface of a conducting material. It can be shown that,

$$\delta_s = \frac{1}{\alpha} = \sqrt{\frac{2}{\omega\mu\sigma}}, \tag{2.32}$$

where δ_s is the skin depth, α is the *attenuation constant*, ω is the angular frequency, μ is the permittivity of the conducting material and σ is the conductivity of the material.

The skin depth for copper at a frequency of 10 kHz is 0.66 mm, and that at 10 MHz is 0.02 mm [20]. Thus, the fields essentially vanish inside copper after traveling a certain distance. This shows the existence of surface current at the boundary of a good conductor.

The practical consequence of this fact is that only a thin plating of good conductor is necessary for low-loss microwave components. But when the thickness of the thin plating comes close to or less than the skin depth, then it leads to high resistive losses in the conductor. In this work, inkjet printed conductive materials are used for the construction of antennas carrying ultra high frequency current. These materials are not as conductive as bulk copper and are having thickness which is only a fraction of the skin depth. This leads to high resistive losses in inkjet printed antennas leading to lower antenna efficiency.

2.8 Passive UHF RFID Tags

RFID tags were first introduced in the early 1970's to enable the passive identification and tracking of inventory for supply chain management, access control, and real-time location systems (RTLS) [27]. The basic principles behind the operation of an RFID tag, which were in use in the battlefields of World War I, is the use of back scattered radio wave for identification [15]. The principle of communication by means of reflected power was later laid out by Stockman in [49]. Later the formal theory of electromagnetic scattering by antennas was initially laid out in [22] and formalized in [23].

With the fundamental principles outlined above there are several different kinds of RFID systems. In this section, some background regarding passive UHF RFID tags are provided which is the relevant topic as far as this thesis is concerned. Figure 2.4 provides an overview of the passive UHF RFID system involving an RFID tag and an RFID reader. The communication between the reader and the tag happens by way of modulated back scattered electromagnetic waves by the tag. The RFID tag is able to harvest energy from the reader, by way of wireless power transfer from the reader device, in order to power itself up and communicate with the reader. Such RFID tags operating in the UHF ISM band (902-928 MHz for North Amercias and

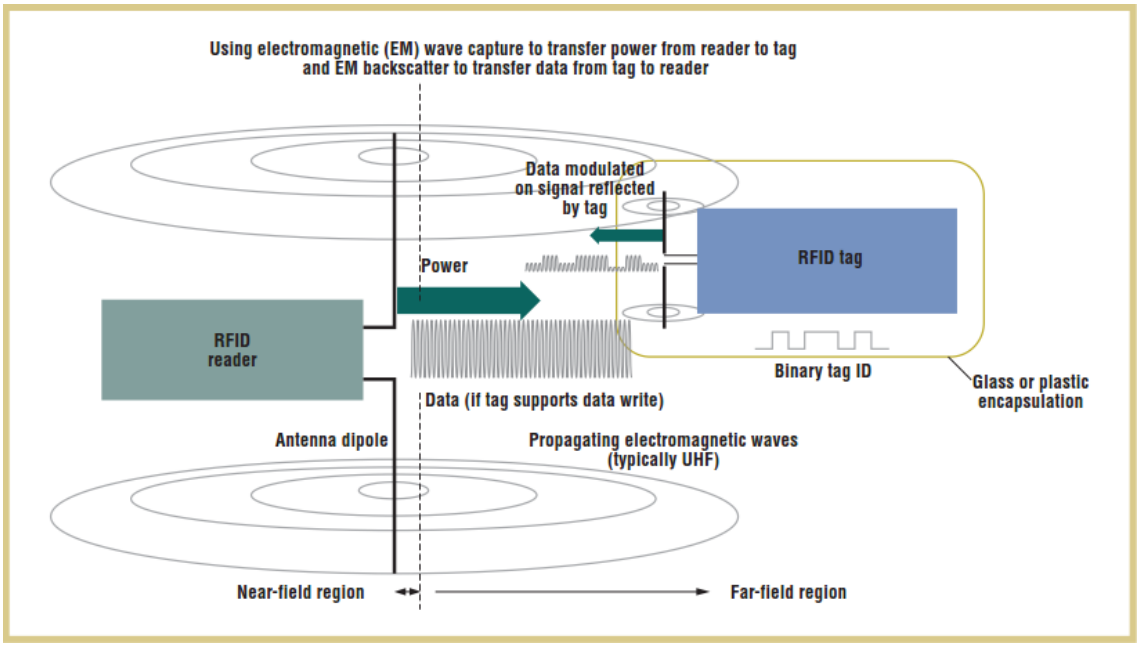

Figure 2.4 *Overview of an RFID system involving an RFID reader and tag [65].*

865 - 868 MHz for EU [15]) would typically provide operation in the range of up to 10 m.

An RFID tag is simply an antenna and a microchip. The microchip contains some memory where a 96-bit electronic product code (EPC) is stored. The EPC code is used to identify or tag an object. There are two key aspects in the operation of an RFID tag, energy harvesting and modulated back scattering.

Energy Harvesting : Passive, or battery free, operation of an UHF RFID tag is realized by harvesting energy from the RF signal transmitted by the reader device. Energy harvesting involves receiving RF energy through the antenna, rectification for RF to DC conversion and then storing the energy in a capacitor. The stored energy in the capacitor is used to drive the circuitry that performs communication with the reader. Efficiency of RF to DC conversion by the rectifier is a key challenge in energy harvesting. It depends on the impedance of the source driving the rectifier. Thus the impedance matching network between the antenna and the rectifier circuit becomes quite crucial to improve the efficiency of the energy harvester. Due to the non-linear nature of the rectifier circuit, optimum source impedance for RF to DC conversion efficiency depends on the input signal level. Hence the optimum impedance match between the antenna and chip is achieved for the lowest power level required to activate the chip [10]. The power transmission coefficient or mismatch loss between the tag antenna and RFID chip varies for higher power levels received by the antenna making the operation of an RFID tag, non-linear.

Modulated Back Scattering : Modulated back scattering focuses on the communication link from the tag to the reader. The theory of loaded scatterers [23] shows that the electromagnetic scattering of radio waves from an antenna depends on the load it is connected to. By varying the load, that is connected to the tag antenna terminal, an RFID tag is able to modulate the reflected electromagnetic wave with binary data [9]. The RFID chip varies the load that is connected to the tag antenna according to the data that it wants to transmit.

An overview of the general design principles of an RFID tag can be found in [42]. One of the key challenge in the design of an RFID tag is to achieve the optimum impedance match between the tag antenna and the RFID chip. Due to the voltage filtering and energy storage, achieved using big capacitors, the input impedance of the RFID chip is highly capacitive. For conjugate impedance matching, this mandates the impedance of the tag antenna to be highly inductive. This requirement is usually

constrained by the size of the tag antenna. Several different impedance matching techniques to overcome this issue are outlined in [28]. The popular impedance matching technique of using T-match network is further explored in [44].

The nature of communication by electromagnetic waves opens up the possibility of identifying multiple objects simultaneously without the need for line of sight, as in the case of optically scanned bar-codes. This feature makes RFID tags attractive for various applications like supply chain management, automated traffic toll collection etc. There were several privacy concerns, raised by many activists, that seemed to have some impact on slowing down the widespread use of RFID tags [3]. RFID chips like UCODE DNA, from NXP Semiconductor, are major steps toward achieving more secure and authenticated usage of tags. The major reason that prevents the usage of RFID tags, if its absent in your local superstore, is predominantly the cost of RFID tags. Though the cost of an RFID tag is around 10 Cents, it is still not economical enough to the value that it brings in.

2.8.1 Tag Performance

One of the key performance parameters of an RFID tag is its read range. The same metric expressed in other words is the threshold power of the tag. These terms are briefly explained in the following sections.

2.8.1.1 Threshold Power

Threshold power is the minimum power required to be transmitted by the RFID reader in order to activate the tag and communicate with it.

Using the Friis transmission equation given in equation 2.31 we shall express the turn on power required to activate the RFID chip as,

$$P_{chip} = \left(\frac{\lambda}{4\pi R}\right)^2 . G_{rTg} . G_{Rdr} . \eta_P . P_{Th}, \tag{2.33}$$

where P_{chip} is the chip turn on power, G_{rTg} is the realized gain of the tag, G_{Rdr} is the gain of the reader and P_{Th} is the threshold power.

$$P_{Th} = \frac{P_{chip}}{\left(\frac{\lambda}{4\pi R}\right)^2 . G_{rTg} . G_{Rdr} . \eta_P} \tag{2.34}$$

It should be noted from the above equation that the threshold power of the tag depends on the distance between the reader and the tag. Hence its not a figure of merit having any absolute meaning.

2.8.1.2 Read Range

One of the most important characteristics of RFID tag is its read range. One limitation on the range is the maximum distance at which tag receives just enough power to turn on and scatter back. Another limitation is the maximum distance at which the reader can detect this scattered signal. The read range is the smaller of the two distances. Typically, reader sensitivity is high enough so read range is determined by the former distance [43].

In other words, read range is limited by the maximum power that an RFID reader is allowed to transmit and the minimum power required by the RFID chip to harvest enough energy, to power itself. The maximum power that an RFID reader is allowed to transmit is defined by regulatory authorities, as the maximum EIRP. For the EU region, the maximum allowed EIRP is limited to 3.28 W and for North America it is 4 W.

Equation 2.33 shall be modified to find the read range of an RFID tag. With the reader and tag antennas having no polarization mismatch, $\eta_P = 1$, and using equation 2.24 in equation 2.31 gives us the read range as,

$$R_{range} = \Big(\frac{\lambda}{4\pi}\Big)\sqrt{\frac{G_{rTg}.EIRP}{P_{chip}}}. \tag{2.35}$$

Theoretical read range measurements could be made at a closer distance using a calibrated measurement setup. Path loss involved in the setup is measured during the calibration of the setup. Subsequently, the read range shall be computed using,

$$R_{range} = \Big(\frac{\lambda}{4\pi}\Big)\sqrt{\frac{EIRP}{L_{path}.P_{th}}}, \tag{2.36}$$

where L_{path} is the calibrated path loss and P_{th} is the threshold power required to activate the tag.

2.9 Sensor Tags

The potential of RFID tags as an energy efficient and miniature wireless sensor node was identified quite early on. It is interesting to note that the author, Roy Want, wrote about ubiquitous sensing using RFID [64] as early on as 2004, which is two years before he wrote an introduction to RFID technology [65]. There are several different sensing paradigms using RFID technology [30]. The early approaches were to have a separate sensor plugged into an RFID tag platform and use modulated back scatter to communicate and collect the sensor data. The self-sensing RFID platform proposes another approach by which the sensor modifies the modulated back scatter signal quality. Self-sensing RFID tags provide zero-power sensor nodes [13] that can be thought of as smart skins [12] to create intelligent environments.

The underlying principle behind self-sensing RFID tags is that any modification in the properties of the antenna or the impedance matching network can be sensed by the RFID reader by the processing of back scattered signals. A thematic block diagram of such a sensor is shown in figure 2.5. The basic theory behind self-sensing RFID tags was initially proposed in [29]. The principles, methods and classification of passive UHF RFID based sensors are extensively covered in [35]. Typically a sensing material, any material that changes its dielectric or conducting properties in the presence of a sensing parameter like temperature [58], humidity [57],[19] or gas [67], [36] concentration, is placed on or close to the tag antenna or its impedance matching network to create a self-sensing passive RFID tag. Another approach is that the sensing parameters like strain [24] or displacement [7] modifies

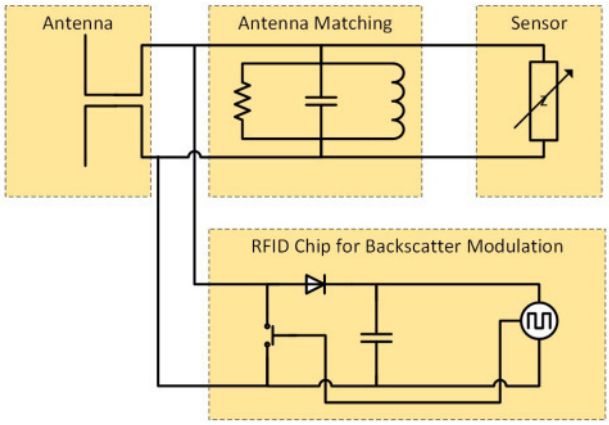

Figure 2.5 *The block diagram of a self-sensing passive UHF RFID tag where the sensor modifies the properties of the antenna or the impedance matching network [13].*

the tag antenna itself and hence its properties. Typically, the threshold power value, or back scattered signal power values are used to make sensing measurements. Additional signal processing leads to several other types of measurement methods for self-sensing RFID tags [35].

2.9.1 Lack of Reference

An RFID tag antenna would behave differently when it is placed in different environments with different dielectric and conductive properties. This affects the performance of an RFID sensor tag. The modulated back scatter properties or the threshold power value that is used to measure a sensed parameter is entrenched in a lot of other variations due to the path loss, multi-path, and fading conditions in the propagation environment. These real life conditions pose severe restrictions to the usage and accuracy of these sensor tags. Having a reference measurement from the sensor tag gives a more robust method which allows the user to maintain accuracy in different measurement scenarios and minimize user created errors.

A dual port temperature sensor shown in [60] tries to address this issue by putting two RFID tags together, where one of it is a self-sensing RFID sensor tag and the other one a simple RFID tag to provide a reference measurement. This method simplifies the sensing measurement and signal processing by the RFID reader as well.

This issue of lack of reference is the key issue that is addressed in the work carried out as part of this thesis work. This thesis proposes another novel approach to provide a reference measurement using only a single RFID chip.

2.10 Carbon Nanotube (CNT)

Carbon nanotubes were discovered by Iijima in 1991 [25]. Carbon nanotubes belong to the family of fullerene structures. There are two types of nanotubes: single-walled carbon nanotubes (SWCNTs) and multiwalled carbon nanotubes (MWCNTs). An SWCNT can be considered as a one-atom-thick layer of graphite rolled up into a seamless cylinder with a diameter of several nanometers, and length on the order of $1 - 100$ microns. MWCNTs consist of multiple layers of graphite wrapped up together to form a tube shape, sharing the same central axis. The structure of

carbon nanotubes provides them with inherently unique electrical, physical, and chemical properties [63].

CNT composites have been found to be one of the most promising materials for gas sensing due to their large surface-to-volume ratio and surface affinity to bond with gasses such as NH_3, CO_2, and NO_x. The combination of the high surface to volume ratio and easy adsorption of these gasses causes significant changes in the electrical impedance of the CNTs upon exposure. Selective functionalization can also be performed to allow CNTs to detect gases individually [12]. In this work, inkjet printable MWCNT based ink called Polyink HC, from Poly-ink [40], is used as the sensing material for CO_2 gas detection.

3. RESEARCH METHODOLOGY AND MATERIALS

This chapter forms the core part of the work done in this thesis. It begins by exploring the motivation behind this work, in the first section. Subsequently, the materials used for this work are laid down. Learning inkjet printing to produce RFID tag antennas was very fundamental to the fabrication of the sensor tag. Hence, one section is devoted to inkjet printing. This section is not an exhaustive guide to inkjet printing, but it covers, most importantly, some of the key parameters optimized, and challenges overcame during this thesis work [1] and prior work [46], [47]. One section is devoted to sheet resistance measurements that helps aligning simulation results and measurement results. The design, fabrication, measurements, results and analysis of the novel CNT sensor tag are covered in the subsequent sections of this chapter.

3.1 Motivation

Wireless sensing using passive UHF RFID is one of the key areas of research for WISE lab at Tampere University of Technology. Humidity sensor [57], strain sensor [24], temperature sensor [58] and dual port temperature sensor [60] are some examples of previous research done at WISE lab in this area. Prior research on wireless sensor using chipless RFID and CNT material for the purpose of gas [53] and temperature [54], [55] is the major source of motivation for the work done in this thesis. The results from these earlier work shows that the property of CNT material to change its conductivity in the presense of certain gases can be used to create sensors with reasonable sensitivity to function as gas detectors. Though wireless gas sensing using inkjet printed CNT material in passive UHF RFID system is already proven [36], [67], this research work, involving inkjet printed CNT inks and passive UHF RFID tag, is pursued to address the problem of lack of reference measurements in sensor tags. This problem is covered in detail in section 2.9.1.

3.2 Materials

Before the design or fabrication of the sensor tag is considered, the materials available for fabrication needs to be considered. Given below is a brief description of the various materials, be it hardware or software.

Fujifilm Dimatix Inkjet Printer. Inkjet printing is chosen as the method of fabrication, as it works well for rapid prototyping. Its availability at WISE and the expertise in inkjet printing gained during past work [46] made it a very natural choice.

Kapton® HN. This flexible polyimide film from Dupont is used as the substrate for printing. It has already proven as a substrate of choice for RFID applications based on past experience within WISE [55], [2]. The dielectric properties of this substrate are also well known, aiding support for computer simulation of any designs.

Harima NPS-JL Ag nanopaste. This silver nano-paste from Harima [21] is an inkjet printable ink with very good conductivity that was also used in the past work [46]. Hence this ink is chosen to fabricate the most conductive parts in this work.

Polyink HC, CNT ink. The most important material of this work is the carbon nanotube (CNT) based ink [40], from French firm Poly-Ink, whose chemical properties enables the functioning of the sensor to be designed. PolyinkHC is an acqueous suspension of PEDOT-PSS and MWCNT.

NXP's UCODE G2iL RFID chip. This is the RFID microchip used in this design [34]. The chip packaging used is SL3S1203FUD/BG which comes with a 7 µm polyimide spacer. The circuit model for this microchip is known from [8], which makes it easier to design a tag antenna that has good impedance matching with the chip.

Voyantic Tagformance Lite. This is the UHF RFID measurement system used in this work to make wireless measurements of the sensor tag. Anechoic measurement chamber, and wideband kit from Voyantic are also used for measurements.

Anysys HFSS v15.0. This electromagnetic, full wave, 3D simulation tool from Anysys is used for simulation and optimization of the RFID sensor tag. The much simpler, free to use, and NEC based antenna modeler and optimizer tool, '4NEC2 ' [4] is also used for some of the initial simulations.

In addition to this other software components like Microsoft Visio, Microsoft Paint and the GNU Image Manipulation Program (GIMP) v2.8 (free and open source image editor) [18] are used in creating the images required for inkjet printing.

This thesis document is prepared using LaTeXword processor using editor TeXstudio and tools from TeXLive. Gnuplot is used to make all the plots in this document.

3.3 Inkjet Printing

Inkjet printing is a type of computer printing that recreates a digital image by propelling droplets of ink onto paper, plastic or other substrates. For several decades, Inkjet printing has been used to print documents and images from a computing environment to paper or similar materials. The need for flexible electronics led to the advent of printing conductive materials on very thin and flexible substrates [45]. Inkjet printing using conductive materials is a proven fabrication method for microwave circuits [5] and RFID tags [51], [26].

Inkjet printing is a purely additive fabrication method. An image of the design to be printed is fed to the inkjet printer. Drop on demand (DOD) technique is used to get the desired pattern on the substrate. The ink drops are jetted only at the locations where metallization is needed, as shown in figure 3.1. Inkjet printing allows usage of extremely thin and flexible substrates like paper, plastic etc. It is well suited for rapid prototyping in the lab, and as a manufacturing technology that is scalable via roll-to-roll processing. Unlike in traditional fabrication methods, involving photo-lithography and etching for patterning, inkjet printing avoids any wastage of materials. As no hazardous chemicals are used, environmental impact due to inkjet printing is minimal.

Inkjet printing using conductive materials, for the production of electronic circuits or antennas, is enabled by the advent of nano-particle based inks. The nano-particle based inks contain nano-meter sized particles of metals like Silver (Ag), Copper (Cu), Gold (Ag) etc. Carbon based materials like Grahene or Carbon Nanotubes are also available for inkjet printing. These nano-materials are mixed with a solvent to create the ink. The solvent is used for stabilization and prevention of coalescence. The nano-material based inks are capable of being used with piezo-electric print heads having micrometer sized nozzle meniscus.

The solvent is removed after printing to achieve solid conductive surfaces. Drying

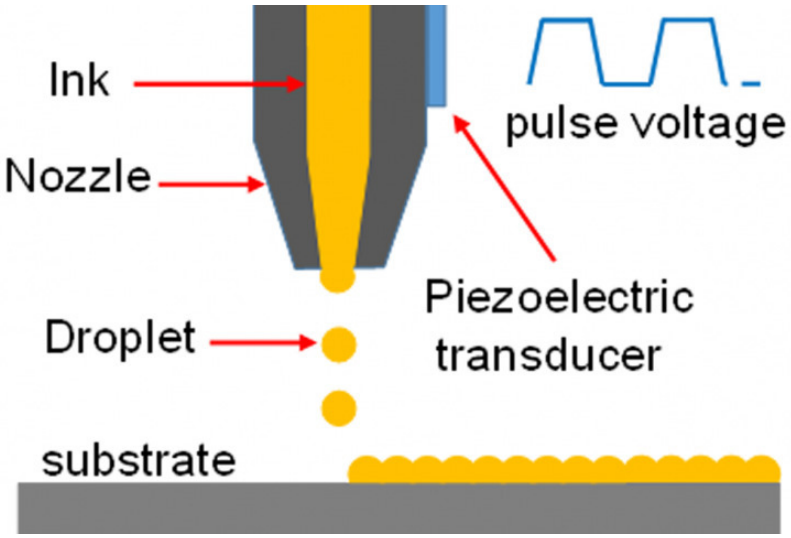

Figure 3.1 *An illustration of the working principle of inkjet printing [37].*

after printing can help remove the solvent. But in order to achieve better conductivity, a sintering process is required. During the sintering process, solvent is removed and the metallic nano-particles are partially melted and fused together. Sintering, in addition to achieving better conductivity, also helps achieving a stable printed pattern that could be subjected to various environmental stresses.

Nano-particles pose environmental safety issues that are probably not well understood [61]. The solvents used with the ink should be carefully handled. Adequate steps are taken in the handling and printing, as per the material safety data sheet (MSDS) of the ink. There aren't any known environmental safety concerns about solid printed patterns resulting from inkjet printing.

The inkjet printer used in this work is the Fujifilm Dimatix materials printer, DMP-2831 [17] [16]. Cartridges capable of producing 10 pl size drops are used for printing. The print cartridge has 16 nozzles capable of jetting ink. Dimatix Drop Manager software is used to control the printer. As discussed in the previous section, a silver nano-particle based ink, Harima NPS-JL [21], is used to produce highly conductive patterns and Poly-ink HC [40], a CNT based ink, is used to create the sensing parts of the sensor tag.

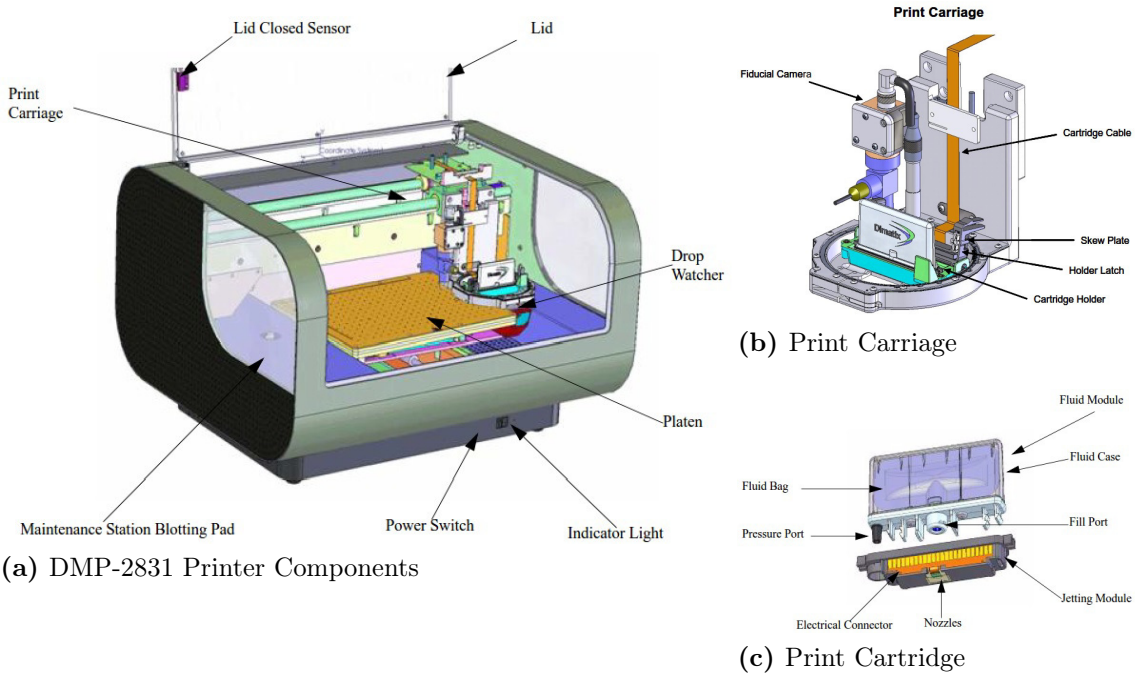

(a) DMP-2831 Printer Components

(b) Print Carriage

(c) Print Cartridge

Figure 3.2 *Fujifilm Dimatix Inkjet Printer DMP-2831 and its key components [16].*

3.3.1 Key Parameters for Inkjet Printing

In this section some of the key parameters that influences the print outcome is discussed. Most of these parameters are optimized using, and applied to, the Dimatix Drop Manager software. For a preliminary discussion, of some of these parameters, the user manual of DMP-2831 [16] is a good resource. But this section will cover some further understanding and techniques, learned during the work in [46], and used during this thesis work. A diagram of the inkjet printer DMP-2831, the Print Carriage, Print Cartridge and its components are shown in figure 3.2.

Most of the parameters discussed here depends on the ink that is used, rather than the printer. Ideally, the ink manufacturer would have fine tuned these parameters on a similar printer. In case of the Ag-ink, NPS-JL there wasn't any such information available from Harima, the manufacturer. In case of the CNT-ink, Poly-Ink HC, optimized parameters for DMP-2831 were provided, in the form of cartridge settings file and waveform file. Table 3.1 summarizes the parameters for both of these inks and a brief description of them is provided in the following sections.

3.3.1.1 Jetting Voltage

The jetting voltage controls the piezo-electric actuators at the nozzles of the cartridge and helps jetting the ink drops. Good quality drops are formed by using proper jetting voltage. The jetting voltage of an ink mainly depends on its viscosity [16]. The drop velocity of the drop can also be increased by increasing the jetting voltage. There are independent jetting voltage controls for each of the 16 nozzles in the cartridge. Jetting voltage of 28 V mentioned in the TABLE 3.1 above, for NPS-JL ink, is an average value, but the voltage for each nozzle will vary slightly to have uniform drop velocity for all nozzles.

3.3.1.2 Drop Velocity

Drop velocity is the velocity of the ink drop, falling from the cartridge nozzles to the substrate, kept in the platen. Drop velocity can be measured using the 'Drop Watcher' feature. The drop watcher window provides a distance scale. It also captures still images after a given time from when the ink is jetted from the nozzle, called 'Drop Refresh Rate'. Using the drop refresh rate and distance scale, the velocity of the drop can be computed. Since the nozzle could be aligned differently due to the cartridge angle, it is important to perform calibration of the nozzle view. 'Calibrate Nozzle View' is used to align all the jets to zero in the distance scale, before measuring drop velocity. Jetting voltage is primarily used to control the drop velocity. Other factors like cartridge temperature could also affect drop velocity. The printer user manual [16] recommends using about 8 - 9 $m\,s^{-1}$ of drop velocity.

Table 3.1 *Key paramters for Inkjet printing*

Parameter	**NPS-JL ink**	**Polyink-HC**
Jetting Voltage	28 V	30 V
Jetting Frequency	5 kHz	5 kHz
Cartridge Temperature	40 °C[#]	28 °C
Platen Temperature	60 °C[#]	38 °C
Drop Spacing	40 µm	15 µm
Pattern Resolution	635 DPI	1693.33 DPI
No. of Printed Layers	2	5

[#] For the first layer of printing, Cartridge temperature of 30 °C and Platen temperature of 40 °C are used. See section 3.3.2.3 for more details.

(a) Waveform of HPS-JL ink.

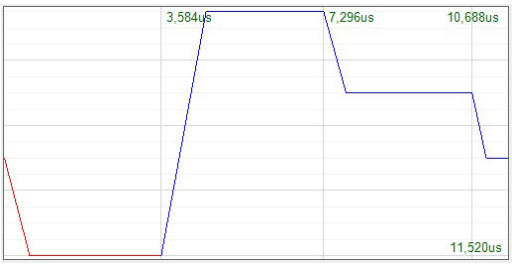

(b) Waveform of Polyink HC ink.

Figure 3.3 *Jetting waveforms used for the inks used in this work.*

This was used for NPS-JL Ag ink. For CNT ink, the drop velocity was much higher while using the setup given by the ink manufacturer, Poly-Ink.

3.3.1.3 Jetting Waveform

The jetting waveform shows time variation of the scaling of jetting voltage applied to the piezo-electric actuators at the nozzles of the cartridge. The optimized jetting waveform for NPS-JL ink and the waveform for CNT ink received from Poly-Ink are shown in Figure 3.3.

3.3.1.4 Jetting Frequency

Jetting frequency decides the rate at which jetting waveform is applied to the piezo-electric actuators. Higher the jetting frequency, faster the printing. But using higher jetting frequency affects the quality of ink drops and print outcome. During printing, the printer uses the maximum jetting frequency, specified along with waveform data. While examining drops in drop watcher lower frequencies can be chosen. But, it is important that the jetting voltage and hence the drop velocities are optimized at the maximum jetting frequency.

3.3.1.5 Cartridge Temperature

Cartridge temperature is the temperature applied at the nozzles. This is used to control the viscosity of the ink. If the ink is too viscous to jet, the viscosity can be lowered by raising the temperature to get the desired jetting performance. It

is important to take notice of the cartridge temperature measurements displayed during printing. If the temperature gradient between cartridge temperature and platen temperature is quite high, then the cartridge temperature could rise due to heat from platen, especially when the printing duration is long.

3.3.1.6 Platen Temperature

Platen temperature is the temperature of the platen (Figure 3.2) where the substrate is kept. Higher platen temperature allows faster drying of the ink. Highest possible platen temperature is 60 °C with DMP-2831. The substrate with the printed pattern is kept on the substrate for 5 to 10 minutes, after completing the printing, in order to help drying the ink, before taking it to actual thermal sintering. If needed, the platen temperature could be kept low during printing and it could be raised after completing the printing.

3.3.1.7 Drop Spacing

Drop spacing specifies the spacing between the drops jetted from the cartridge. In other words, it defines the pattern resolution of the print outcome. Good drop spacing would provide good conductive printed pattern with uniform thickness and good definition. Lower drop spacing means lower amount of ink, and it could cause discontinuities in the printed pattern. Higher drop spacing implies higher quantities of ink per unit area, but it could cause flow of ink on the substrate, which leads to poor definition at pattern boundaries and non uniform thickness of the pattern.

Drop spacing or pattern resolution depends on the nature of the ink and the substrate to which it is printed. A drop size test is done to find the optimum drop spacing. A drop matrix printed on Kapton substrate using NPS-JL ink is shown in Figure 3.4. This drop matrix is printed with the highest possible drop spacing of 254 µm. A microscope is then used to measure the area of each drop from which an average drop radius is found out. For NPS-JL, the average drop radius is around 45 µm.

Ideally, one would choose drop spacing equal to the drop radius to achieve good conductive pattern with uniform thickness. At the very least, drop spacing equal to the drop diameter could be used to give a continuous conductive pattern. A drop spacing lower than the drop radius could be also employed to achieve higher effective

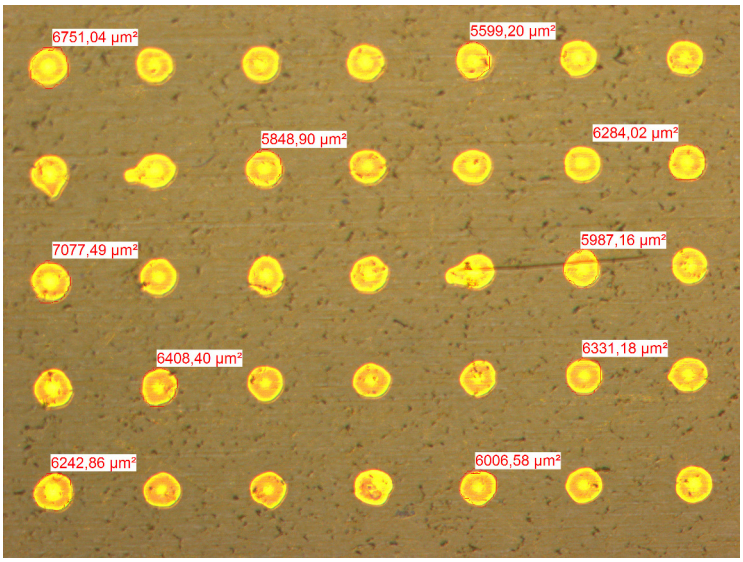

Figure 3.4 *A microscopic image of the drop matrix printed on Kapton substrate printed using NPS-JL Ag ink. The measured drop area of some of the drops is shown as well.*

thickness. In this work, a drop spacing of 40 µm is chosen, for NPS-JL ink, which is equivalent to pattern resolution of 635 DPI. For Polyink HC ink, drop spacing of 15 µm or pattern resolution of 1693.33 DPI is used as recommended by Poly-Ink.

3.3.1.8 Number of Printed Layers

One of the key advantages of inkjet printing is the possibility to print multiple layers of the same pattern. This helps reducing the sheet resistance by increasing the thickness of pattern. Increased sheet resistance reduces conductive losses, and thus helps improving the read range of the RFID tag [56],[31]. More advanced techniques like selective ink deposition can help improve the read range minimizing the consumption of the ink [48], [59].

In this work, two layers of NPS-JL ink are printed for the Ag ink pattern and five layers of Polyink HC ink are printed to make the CNT ink pattern, as shown in TABLE 3.1. Printing multiple layers could be done with or without an intermediate sintering process, in between. In this work, sintering for Ag ink is performed after printing the two layers at once. Similarly, the five layers of CNT ink are printed at once and sintering is performed afterwards.

3.3.2 Key Challenges of Inkjet Printing

The previous section discussed several parameters associated with the inkjet printer, that needs to be optimized to achieve good pattern quality. In addition to this, there are several challenges associated with inkjet printing, that further adds complexity to the printing process. Some of these challenges are briefly covered in this section. Most of these challenges are primarily due to the ink quality. Even the same ink, but from a different batch of production, can have slightly different printing performance.

3.3.2.1 Functioning Nozzles

The printer cartridge contains 16 nozzles in total. Using more nozzles will increase the speed of printing. It is necessary that all the nozzles chosen for printing are close to each other with no non-functioning nozzles in between. Unfortunately, not all the nozzles would be functioning properly with good drop formation. The necessity to find contiguous working nozzles restricts the amount of nozzles that could be used. This impacts the speed of printing especially while using higher pattern resolution or lower drop spacing.

3.3.2.2 Cartridge Angle

The printer achieves the required drop spacing in the horizontal direction (along X-axis) by the physical movement of the print carriage. The cartridge could be kept at different angles within the print carriage. The angle at which the print cartridge is kept on the print carriage decides the drop spacing in the vertical direction (along Y-axis). So in addition to specifying the required drop spacing in the Drop Manager software, one need to setup manually the appropriate cartridge angle corresponding to the drop spacing.

The cartridge angle setup is prone to various errors, as the cartridge angle is a manual setup that is physically setup using a vernier scale provided on the print carriage. Drop Manager software provides a cartridge angle calibration feature which allows one to measure and correct the required drop spacing by adjusting the angle. This process uses the distance between two horizontal lines created by jetting from the two nozzles at the ends of the chosen set of nozzles. This process remains challenging

with inks that have bigger drop radius and hence do not create fine lines. Also, if the ink is transparent like Poly-Ink HC, that doesn't yield to this calibration process as well.

This error in the cartridge angle would mean improper drop spacing in the vertical direction when compared with the horizontal direction. This would cause different thickness in vertical tracks of the pattern when compared with the horizontal tracks. The error also creates skirt line pattern on vertical line edges as shown in figure 3.6. While printing it is always better to keep the longer portions of the pattern horizontally, to have better pattern resolution, and to improve the speed of printing.

3.3.2.3 Wetting Performance

The contact angle of the ink with the substrate is very important to have good adhesion and wetting performance [32]. The contact angle depends on the viscosity of the ink and the surface energy of the substrate. Kapton substrate has hydrophobic nature and the water based ink like Polyink HC creates quite a high contact angle that prevents adhesion of the ink. Oxygen plasma treatment was done on Kapton surface to reduce the contact angle and hence improve wettability [66], [2].

In order to print Polyink HC, Kapton samples were treated with oxygen plasma using Diener PICO plasma cleaner (Diener Electronic GmbH + Co. KG, Germany). The plasma cleaner is equipped with 13.56 MHz frequency generator and reactive ion etching electrodes. Samples were exposed to oxygen plasma for 2 minutes in 0.3 mbar pressure using 30 W power with 3 sccm oxygen flow rate. Figure 3.5 shows the improvement in wetting performance observed.

With the NPS-JL Ag ink, the wetting problem was found to be the other way around, such that Kapton was highly hydrophilic to the Ag ink. This causes a very low contact angle and the ink would flow from substrate. This cause poor definition of the pattern as shown in Figure 3.6e. When a second layer is printed on top of printed pattern, then the definition was found to be very good. Since there is no surface treatment to increase the contact angle, the cartridge temperature was reduced to increase the surface tension of the liquid. Cartridge temperature of 30 °C and platen temperature of 40 °C is used for the first layer. This is an exception to the parameters given in TABLE 3.1. This helped reducing the problem, but not

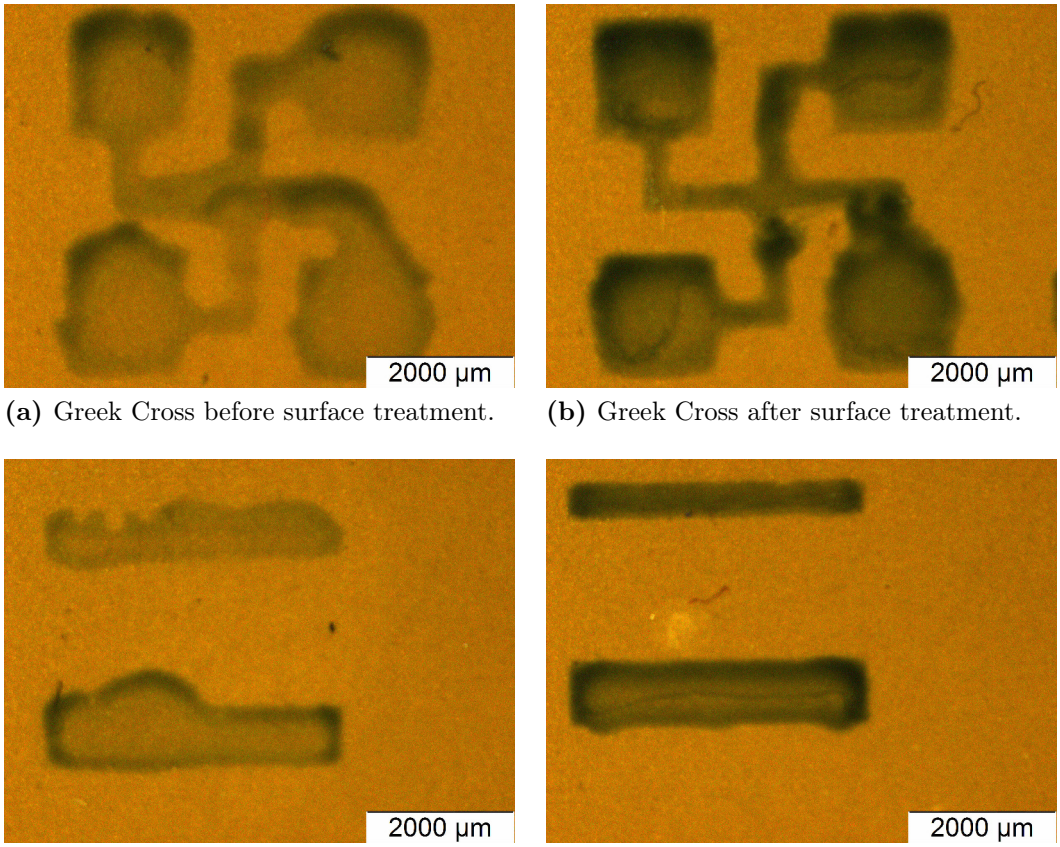

(a) Greek Cross before surface treatment. **(b)** Greek Cross after surface treatment.

(c) Line patterns before surface treatment. **(d)** Line patterns after surface treatment.

Figure 3.5 *Wetting performance of CNT ink before and after surface treatment on Kapton substrate.*

completely removing it. Reducing the pattern resolution to 317 DPI for the first layer and using the normal pattern resolution of 635 DPI to print two additional layers on top, is found to give better pattern definition as shown in Figure 3.6b. While printing the RFID tag, somehow, this method gives poorer antenna efficiency leading to poor read range. Hence printing the first layer with a lower cartridge temperature is found to be the optimum solution.

3.3.2.4 Reference Point

The Dimatix inkjet printer uses a reference point on the digital image, and on the platen in order to properly align printing multiple layers on top of an already printed pattern. The reference point needs to be carefully used, if the final pattern involves printing multiple inks, and different pattern resolutions, which is the case in this

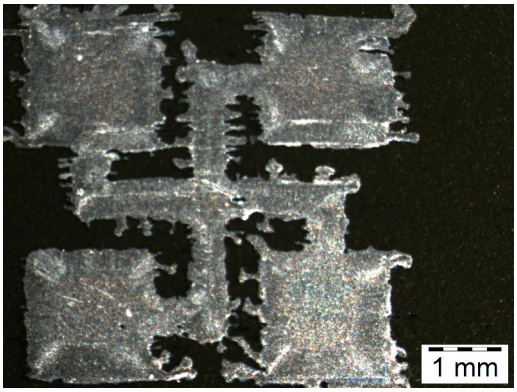

(a) Greek Cross pattern.

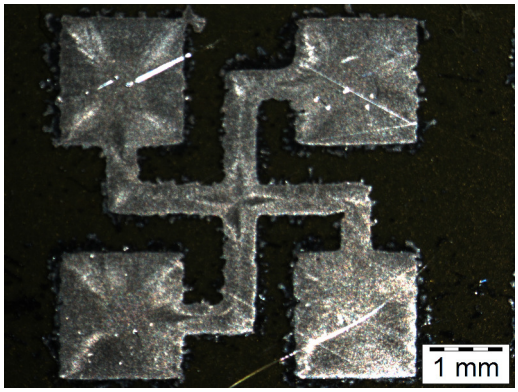

(b) Greek Cross pattern.

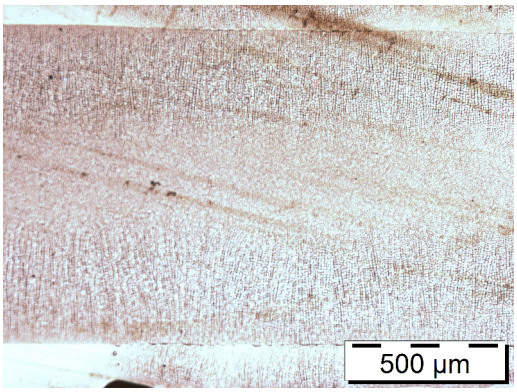

(c) Horizontal line.

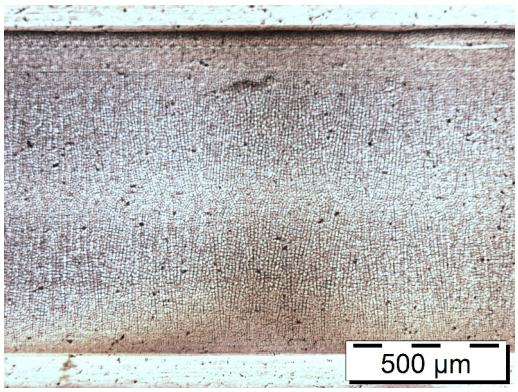

(d) Horizontal line.

(e) Vertical line.

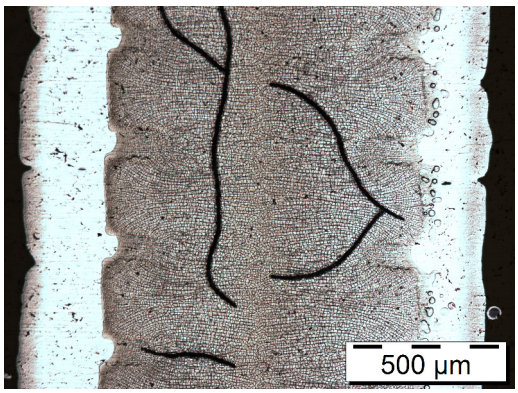

(f) Vertical line.

Figure 3.6 *Wetting performance of Ag ink, without and with using a low resolution base layer of printing. Figures on the left side 3.6a, 3.6c, and 3.6e shows two layers printed with* 635 DPI*, while pictures on the right side 3.6b, 3.6d, and 3.6e shows one layer printed with* 317 DPI *and two layers of* 635 DPI *printed on top of it. Comparison of horizontal and vertical lines also shows the impact of cartridge angle error, causing some skirts on vertical lines.*

work. The fiducial camera in the inkjet printer is used to choose the reference point on the substrate placed in the platen. A reference point is chosen in the pattern file of the digital image. The printer aligns the reference point in the image, to the reference point chosen through the fiducial camera.

Figure 3.7 shows the patterns used in this work. The patterns in figure 3.7a and figure 3.7b are printed on top of each other in alignment, with different inks and different pattern resolutions, to form the complete antenna pattern in figure 3.7c. The antenna pattern originates from the 3D modeling tool in the electromagnetic simulation program. The two patterns are separated from one combined pattern. Before separating the two parts, two extra horizontal lines are added at the top and bottom of the design, as shown in figure 3.7. These extra lines server three different purposes as described below.

1. **Reference Point:** They allow choosing a common reference point, that is at the same position for both the patterns. This allows choosing the correct reference point through the fiducial camera while printing the second pattern. In

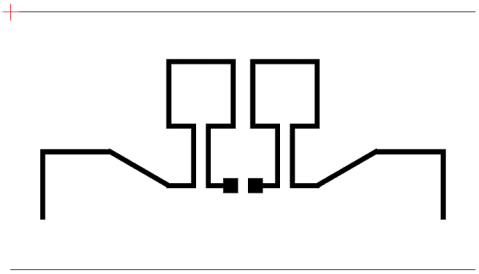

(a) Ag ink pattern at 635 DPI.

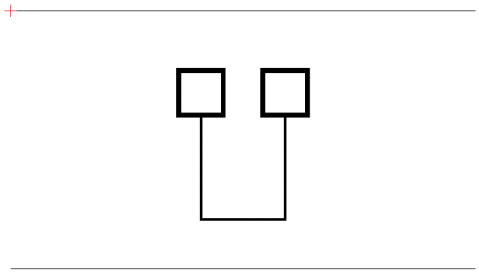

(b) CNT ink pattern at 1693.33 DPI.

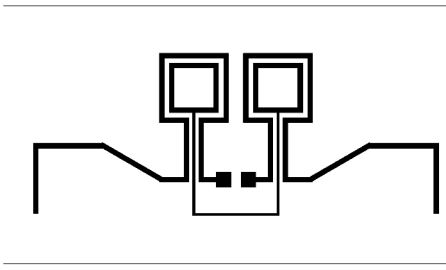

(c) The summed up pattern.

Figure 3.7 *The red cross hair at the top left corner of the top two images (Figure 3.7a and Figure 3.7b) show the reference point that is used to align the top two patterns that needs to be printed separately, to get the final pattern shown below in Figure 3.7c.*

this work, Ag ink pattern is printed first and while printing CNT ink pattern, the reference point on the Ag ink pattern visible through the fiducial camera is chosen.

2. **Tiling:** The horizontal lines form a unique boundary for both patterns creating images of the same size. This allows tiling these patterns, without damaging the alignment, with a single reference point. Multiple copies of the same pattern are printed at once, by tiling the image in the horizontal and vertical directions.

3. **Theta Calibration:** It is important, to place the substrate with no angular tilt, in order to align the pattern to be printed. 'Calibrate Theta' feature in the inkjet printer allows calibration of angular offset by choosing two points on a horizontal line. Before printing the CNT ink pattern, theta calibration is performed using a horizontal line printed with Ag ink.

3.3.2.5 Drop Offset

Changing the cartridge or modifying the cartridge angle would modify the reference point of the inkjet printer. The 'Drop Offset' feature in the inkjet printer is used to calibrate the position of a new or different cartridge to the previous printed pattern. While performing drop offset calibration, the printer prints a 15 mm horizontal line and a single drop 1 mm away from the right end of the line. With the help of the fiducial camera, the operator needs to click on the drop, which completes the calibration procedure. In order to perform this, the visibility of ink on the substrate is necessary.

Due to the transparency of the CNT ink, it is impossible to locate the drop and complete the drop offset calibration. To overcome this, drop offset calibration is performed with the Ag ink cartridge itself, after printing Ag ink pattern. The cartridge angle is modified to correspond to the pattern resolution of 1693.33 DPI and the drop offset calibration is performed with the Ag ink cartridge itself. While printing CNT ink though the cartridge is changed, its angle remains the same, and the lack of drop offset calibration with the new cartridge is found negligible. Figure 3.8 shows the impact of drop offset calibration on the outcome of printing.

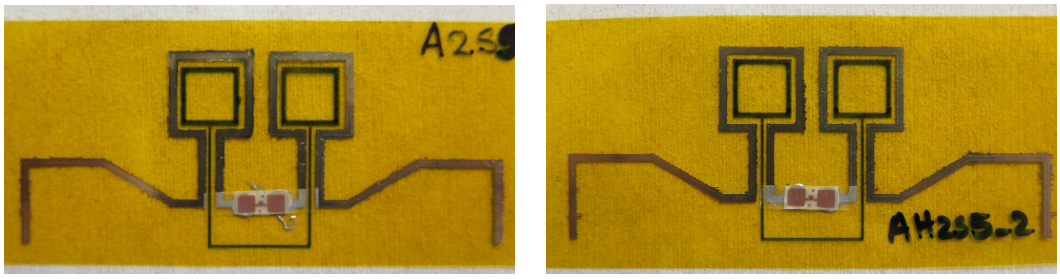

(a) Without drop offset calibration. **(b)** With drop offset calibration.

Figure 3.8 *These pictures of the final printed pattern show the impact of drop offset calibration. The picture on the right has the Ag ink pattern (silver coloured) and CNT ink pattern (black coloured) perfectly aligned as required in the final pattern shown in Fig 3.7c, where as the picture on the left hand side shows the CNT pattern slightly shifted to the left.*

3.3.3 Images for Inkjet Printing

The Dimatix Drop Manager software which controls the DMP-2831 inkjet printer needs an image of the pattern as input. It needs this image in BMP file format. This section details the method used to create such an image. The design dimensions should be preserved from the simulation software, where its conceived, to the print outcome. It is important to do so without any manual manipulations in dimensions, thus reducing the risk of human error. The resolution of the image needs to be the same as the resolution/drop spacing used during printing. The Dimatix Drop Manager software will convert the BMP images to its own pattern file using drop spacing (resolution) as a parameter. So it is very important that the BMP image has the right resolution to avoid any undesired scaling of dimensions.

The printing pattern is originated in the electromagnetic simulation suite, Anysys HFSS. The 3D Modeler portion of this software provides provision to export the design in AutoCAD DXF file format. It is important to keep the design in the XY plane of the Modeler in order to do so. This DXF file format can be inserted into a blank document in Microsoft Visio software. Microsoft Visio is capable of exporting the design as a black and white BMP image with the needed resolution. Unfortunately, the DXF file keeps only the outline of the design and Microsoft Visio is not able to do colour (black) filling inside the design outline. The GIMP software comes to the rescue here, as it is able to open the BMP image, convert the image mode to grayscale and then fill the design outline with black ink. One can inspect the design dimensions and resolution with the help of image properties in GIMP software. GIMP exports the modified image as a BMP image, but is not preserving

the resolution doing so. Hence the image is exported as a JPEG image first. This JPEG image can be opened in Microsoft Paint software and can be saved as a monochromatic BMP image, preserving dimensions and resolution. This image is now ready to be fed as input to the Dimatix Drop Manager software.

The method described above may not be the best approach, especially if one has access to expensive software like ACE Translator 3000 [33] which could directly create BMP images from DXF file formats. The method above is adapted using software that are already available or are open source.

3.4 Sheet Resistance Measurements

It is quite important to know the sheet resistance of the material used, during the simulation and optimization of an RFID tag. This helps obtaining reasonable simulation results for antenna parameters like radiation efficiency, which in turn helps computing RFID tag performance parameters like, read range and threshold power. Obtaining simulation results which are quite close to real measurement results help gaining insight during the design process. Some ink manufacturer might provide the expected conductivity information, but the realized conductivity might be different. Printing with the same parameters on different substrates could lead to different sheet resistance values as well, as shown in [46].

Greek cross structures can be used to obtain an approximate sheet resistance value (within 1 %) [62]. Chapter 2 from [62] describes the method, measurements and calculations that are performed to obtain the sheet resistance value. A pattern file including 8 such greek crosses and a few horizontal and vertical lines of various widths are printed to measure the achieved sheet resistance and thickness. The print outcome and the pattern file are shown in figure 3.9.

The sheet resistance of each of the greek cross is separately measured using a Keithley 2425 four-probe measurement station. The measured sheet resistance was found to be around 80 mΩ/square, for a pattern printed with two layers of NPS-JL Ag ink. The thickness of the square at the center of the greek cross is measured using Veeco Wyko NT1100 optical profiling system. The measured thickness is about 1 µm, for a pattern printed with a single layer of NPS-JL Ag ink.

Sheet resistance measurements were not performed for the CNT ink, Polyink HC. The ink manufacturer, Poly-Ink, provided a sheet resistance value of 15 Ω/square.

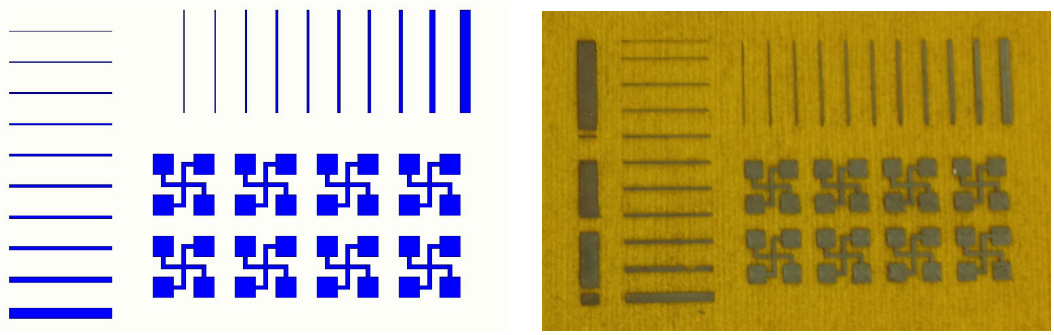

(a) Test pattern created in Drop Manager Software.

(b) Test pattern printed on Kapton.

Figure 3.9 *The above figures show the greek cross pattern created in Dimatix Drop Manager, and the print outcome using this pattern file, on Kapton substrate with NPS-JL Ag ink. Each vertical and horizonatal lines are* 10 mm *long.*

They measured this sheet resistance from printed patterns of 1 µm of thickness, produced by printing 5 layers of CNT ink.

3.5 Design and Simulation

The main motivation behind the design of the sensor tag and the main problem it is trying to address is discussed in section 3.1. Section 3.2 discussed the materials that are available and chosen to be used in this work. The sensor tag is designed to operate in the ISM band for North America, which uses 902 - 928 MHz frequency range. A key aspect in the design of an RFID tag is the impedance match between the tag antenna and RFID chip [28]. Using the circuit model of NXP G2iL from [8], the chip impedance values across various frequencies are computed. The chip impedance at 915 MHz is found to be $Z_c = 12.76 - j192.29\Omega$.

The corner stone of this sensor design is the property of CNT material to change its conductivity in presence of CO_2 gas, as shown in [53]. A typical chemical loading of an RFID tag involves physically placing a sensing material, on top of a typical RFID tag, at the very sensitive part of the tag [35]. This approach leaves no room to have any measurement from the tag that is devoid of influence from the sensing material. In order to achieve a reference measurement, which is the key motivation behind this work, the sensing material needs to be physically separated the actual RFID tag. The effect of inductively coupled loading bars on meandered dipoles for RFID tags shown in [42] and [52] provide the motivation for this kind of design.

Table 3.2 *Dimensions of the sensor tag shown in figure 3.10.*

Parameter	Value (mm)	Parameter	Value (mm)	Parameter	Value (mm)	Parameter	Value (mm)
LT	81.96	L3	14	W1	1	SG	1
WT	32.33	L4	13.65	WS1	0.5	WG1	2
L1	13	LS1	17.5	WS2	1	WG2	1
L2	11	LS2	6.75	FG	1	WG3	3

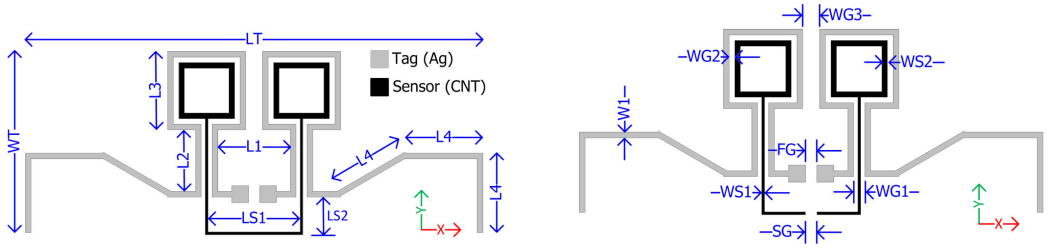

(a) Sensor ON (SON) Mode **(b)** Sensor OFF (SOFF) Mode

Figure 3.10 *Dimensions (values in TABLE 3.2) and materials of the CNT sensor tag. This figure doesn't show the* 50 µm *thick Kapton® HN used as substrate material.*

The final structure of the CNT sensor tag designed with these ideas is shown in figure 3.10 and the dimensions of it are given in TABLE 3.2.

The simulation platform 4NEC2 [4] is used during the initial design stages. The design process starts with a half-wave dipole antenna made of copper wire kept in free space. The dipole is modified to have an inductive loop in its structure for two purposes. First, to have a highly inductive antenna impedance in order to match with the highly capacitive RFID chip impedance. Secondly to have a strong inductive coupling with a loading bar having its own inductive loop. A loading bar in the form of a conductive wire is placed near the dipole. The loading bar is closely coupled to the tag antenna by means of an inductive loop in the loading bar placed inside the inductive loop of the tag antenna. The dipole is given additional meandering and end loading to obtain the required input impedance for the tag antenna. The overall length of the dipole antenna is optimized to obtain the desired antenna impedance at the center frequency of 915 MHz. The design and dimensions obtained from 4NEC2 forms the guideline for the real design in ANYSYS HFSS simulation environment.

The dipole antenna structure obtained from 4NEC2 simulation is recreated in ANYSYS HFSS replacing copper wires with planar conductive sheets. The material Kapton®

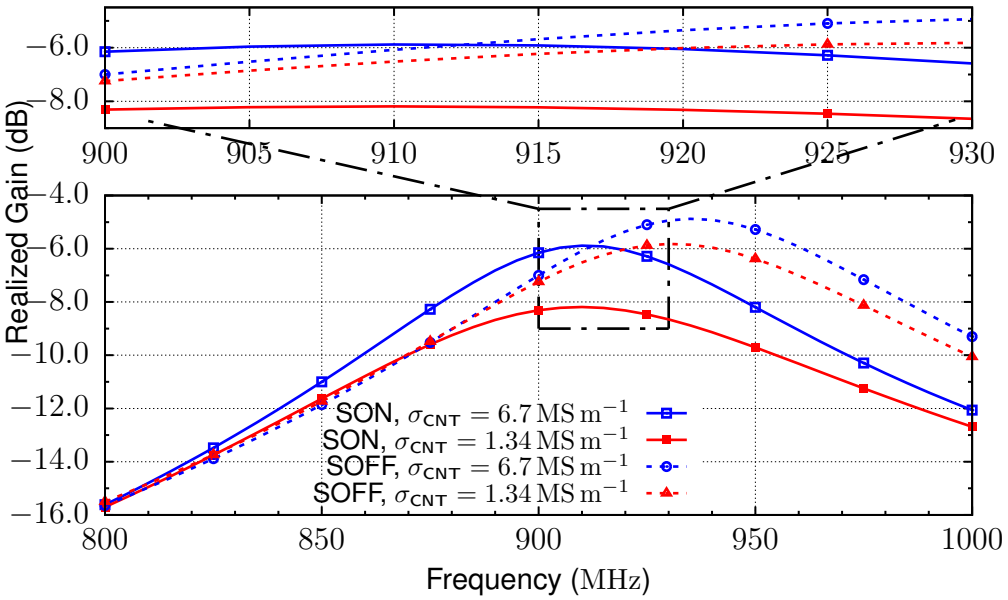

Figure 3.11 *Simulated Realized Gain values vs. frequency in SON and SOFF mode with different conductivity values for CNT. These measurements are along the z-axis with reference to the co-ordinate system shown in figure 3.10.*

HN is introduced as substrate with 50 µm thickness. A new material is introduced in HFSS to model inkjet-printed Ag ink. The conductivity derived from sheet resistance measurements (see section 3.4), is used to define the new material. Similarly a new material using the conductivity value of CNT ink is also introduced. The tag antenna is assigned the inkjet-printed Ag material and the loading section is assigned the inkjet-printed CNT material. Thickness of 1 µm is assigned to both of these conductive sheets. The net length of the tag antenna, keeping the loop dimensions constant, is further modified to obtain the input impedance at the center frequency of 915 MHz. Going forward, the whole design will be called 'CNT sensor tag'. Also, the tag antenna part and loading bar section will be called the 'Tag' and 'Sensor' part respectively.

The conductivity of CNT, the sensor material, is modified to observe its impact on the realized gain of the CNT sensor tag. According to the results observed in [53], the conductivity is reduced 5 times to simulate the sensing performance. The parameters $WG1$, $WG2$, and $WS1$ are modified to get up to 2 dB variation in realized gain of the CNT sensor tag while the conductivity is reduced 5 times. This gives the desired sensing operation. This behaviour is shown by the thick blue and red curves in figure 3.11.

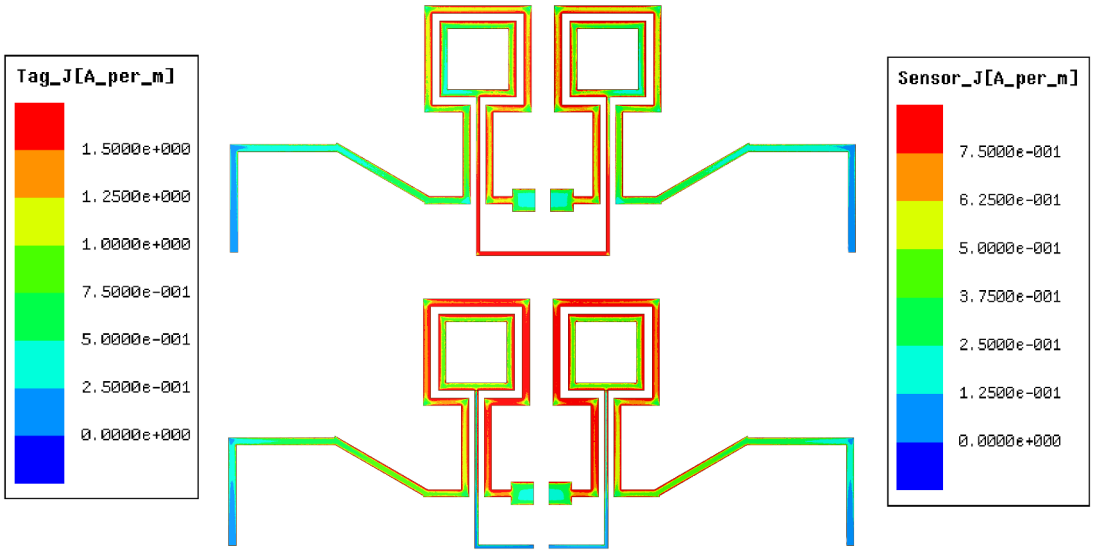

Figure 3.12 *Sensor tag's simulated surface current at SON (above) & SOFF (below) modes, using* $-18dBm$ *input power and source impedance equal to chip impedance, at* $915MHz$*. Sensor's and Tag's currents use different scales.*

3.5.1 Reference Mode Operation

A switch is placed at the centre of the loading section to achieve the required reference mode operation. The CNT sensor tag in the switch on (SON) mode or sensing mode and the switch off (SOFF) mode or reference mode is shown in figure 3.10a and figure 3.10b respectively. The switch, when turned off, disturbs current flow in the loading bar, modifying its effect in the operation of the tag. The current flow, or the lack of it, in the loading bar impacts both the gain and input impedance of the CNT sensor tag.

Impact of the loading bar and the switch in it, is best explained by the surface current diagram of the CNT sensor tag shown in figure 3.12. The surface current plot is made using field overlay plots in HFSS. In order to obtain the exact current magnitudes, input power of -18 dBm (turn on power of the chip[34]) and source impedance equal to chip impedance, is applied to the excitation source. The figure 3.12 shows the current flow in the tag part is very high in SOFF mode. Higher current in the tag part gives higher gain for the CNT sensor tag. But it introduces impedance mismatch, effectively reducing the realized gain of the sensor tag. In SON mode, higher current flow in sensor part loads the tag, reducing gain of the CNT sensor tag. But the power transmission coefficient is higher in SON mode.

This gives higher realized gain for the CNT sensor tag in SON mode.

The dimensions $L1$, $L2$, $LS2$, and $WG1$, shown in figure 3.10, are used in the optimization of the CNT sensor tag. The optimization is performed to achieve two objectives. First is achieving optimum input impedance at 915 MHz in the SON mode operation. Second objective is creating enough input impedance mismatch while the switch in the sensor is turned off, such that the realized gain of the CNT sensor tag doesn't vary significantly, in the frequency range of 902-928 MHz, while the conductivity of the sensor is varied. The result of this is seen in the simulation results shown in figure 3.11. The dashed blue curve in figure shows the increased realized gain in SOFF mode. The maximum realized gain is also shifted in frequency due to the impedance mismatch. As shown in the zoomed plot, the variation of realized gain shown by the dashed blue and red curve is quite small between 900 MHz and 930 MHz. The minor variation of realized gain in SOFF mode provides the needed reference mode operation.

3.5.2 Simulation Setup

The simulation model created in ANYSYS HFSS is shown in figure 3.13. The outer box seen in figure 3.13a indicates the radiation boundaries inside which the electromagnetic field equations are solved. In this simulation model, the symmetry of the design is exploited to reduce the computation time. A symmetry boundary is used in the yz-plane and solutions equivalent to the full model are obtained. The following sections provide further details about the simulation setup.

3.5.2.1 Modeling

The tag and sensor part of the design is modeled using sheet materials of designed dimensions. The terminal of the tag is modeled according to the packaging type (SL3S1203FUD/BG) of the RFID chip. The port used to provide excitation is defined using rectangular sheet. The substrate, Kapton, is modeled using a 3D box having dimensions 52 mm × 52 mm × 0.05 mm. The radiation boundary is created using another 3D box. The dimensions of this box are chosen to be half wavelength wide in all directions except along the x-axis where quarter wavelength is used due to the symmetry boundary on the yz-plane.

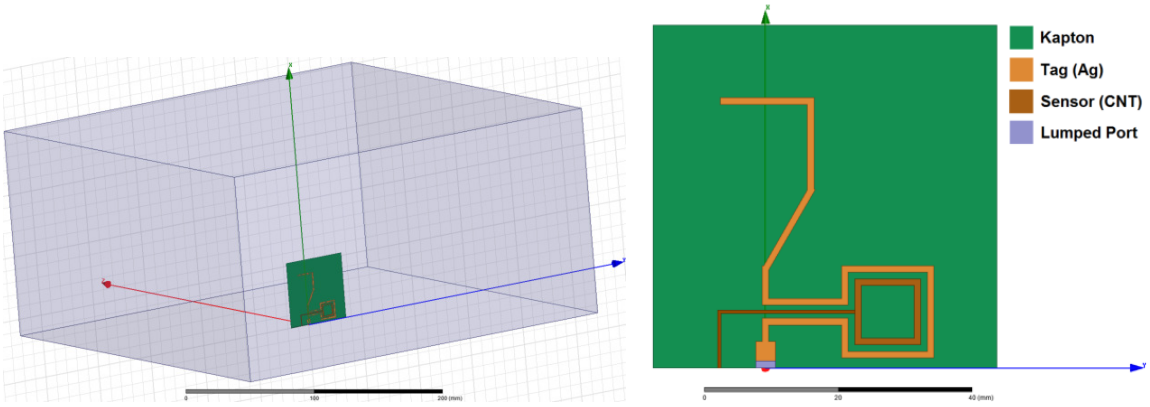

(a) Simulation model including the boundaries **(b)** A closer look at the simulation model.

Figure 3.13 *The simulation model created in ANYSYS HFSS.*

3.5.2.2 Materials

The substrate, Kapton, is modelled using a dielectric material of relative permittivity, 3.4 and loss tangent, 0.0055. Inkjet-printed Ag material and CNT material are modelled as conductive materials with conductivity of $1.23 \times 10^7\,\mathrm{S\,m^{-1}}$ and $6.7 \times 10^6\,\mathrm{S\,m^{-1}}$ respectively. Sheet resistance measurements, explained in section 3.4 is used to derive these conductivity values. Vaccum material from HFSS material library is assigned to the boundary box.

3.5.2.3 Ports

A lumped port is assigned to the rectangular box drawn as port and shown in figure 3.13b. A source impedance of $50\,\Omega$ is applied. The integration line of the lumped port is drawn in the direction of x-axis shown in figure 3.13b.

3.5.2.4 Boundaries

Layered impedance boundary is used to define the tag and sensor part of the design. Thickness of $1\,\mu\mathrm{m}$ is used for both of these sheet materials. Radiation boundary is assigned to all the faces of the boundary box except at the yz-plane. Perfect E-symmetry boundary is applied to the face of the boundary box in the yz-plane. A port impedance multiplier of value 2 is used because the model has one-half of

the voltage differential and one-half of the power flow of the full structure.

3.5.2.5 Meshing

Meshing operations, based on element length, are specified for the tag, sensor and kapton substrate. The substrate mesh is given a maximum element length of 3 mm. Maximum element length of 0.5 mm is used for meshing the 1 mm wide sections of tag and sensor parts, while the narrower tracks of sensor part are given 0.25 mm meshing.

3.5.2.6 Solution Setup

A driven model solution setup is used to compute full wave solution to the model created. 900 MHz is set as the solution frequency. A maximum Delta S value of 0.02 is used as convergence condition for the simulation. A minimum number of two converged passes is set as a requirement. An iterative solver using first order basis functions with a relative residual of 0.0001 is chosen as solution options. Lambda refinement with the default lambda target of 0.33 is chosen for initial mesh options. A discrete sweep setup is defined from 0.8 GHz to 1 GHz, with frequency step of 5 MHz. The setup is made to save all field values. In order to obtain far field antenna patterns and other solutions depending on it, an infinite sphere setup is added as a radiation surface.

3.5.2.7 Output Variables

Custom output variables listed in TABLE 3.3 below is used to compute certain sensor tag performance parameters as given in the table. Some variables are related to the equivalent parallel RC - circuit model of RFID chip from [8]. Others are user defined constants, constants and variables defined in the simulator, variables holding simulation output values and then some key performance parameters like, read range and realized gain derived from all the previous variables. The simulation results are plotted using these output variables. Please note that the maximum EIRP value as per EU regulation is used to compute the read range.

Table 3.3 *Output variables defined for simulation.*

Variable	Value	Description
EIRP	3.28	Maximum EIRP by EU regulation.
P_{chip}	$10^{-4.8}$ W	Chip turn on power -18 dBm in Watts.
C_{eq}	0.91 pF	Equivalent capacitance from chip model.
C_p	0	Parasitic capacitance from chip model.
R_{eq}	2.85 kΩ	Equivalent resistance from chip model.
R_{chip}	$\frac{1/R_{eq}}{(1/R_{eq}^2+(2\pi(C_{eq}+C_p)f)^2)}$	Resistive part of chip impedance.[1]
X_{chip}	$\frac{-2\pi(C_{eq}+C_p)f}{(1/R_{eq}^2+(2\pi(C_{eq}+C_p)f)^2)}$	Reactive part of chip impedance.[1]
tau_dB	$10\log\left(\frac{4R_{ant}R_{chip}}{(R_{chip}+R_{ant})^2+(X_{ant}+X_{chip})^2)}\right)$	Power transmission coefficient.[1] [3] [4] From equation 2.28
$rGaindB$	$dB(GainTotal)+tau\_dB$	Realized Gain.[5] From equation 2.29
$Rrange$	$\frac{c}{(4\pi f)}\sqrt{\frac{EIRP\times10^{(rGaindB/10)}}{P_{chip}}}$	Read Range.[1] [2] From equation 2.35

[1] f is an internal variable in simulator named 'Freq' indicating frequency.
[2] c is an internal constant in simulator named 'c0' indicating velocity of light.
[3] R_{ant} is the real part of port impedance obtained from simulation output using 're(Z(P1,P1))' which takes the real part of the Z-parameter computed for port P1.
[4] X_{ant} is the imaginary part of port impedance obtained from simulation output using 'im(Z(P1,P1))' which takes the real part of the Z-parameter computed for port P1.
[5] $GainTotal$ is the gain of the sensor tag obtained from simulation output using a variable by the same name.

3.5.3 Simulation Results

As discussed in the previous section, output variables like realized gain and read range derived from simulation output values are plotted to examine the expected results from the model. In addition to this typical antenna parameters like antenna impedance, Gain and radiation efficiency are directly obtained from simulation output. The simulations are performed by parameterizing the conductivity of CNT material by using the values $6.7\,\mathrm{MS\,m^{-1}}$ and $1.34\,\mathrm{MS\,m^{-1}}$. The switch is modelled by removing 0.5 mm long rectangular sheet.

The radiation pattern of the CNT sensor tag is the typical doughnut shaped pattern from a half-wave length dipole antenna.

The antenna impedance obtained using the Z-parameters from the simulation result is shown in figure 3.14. The resistive and reactive part of the impedance is plotted separately. The resistive and reactive part of the chip impedance is plotted along with it for comparison. It can be observed that the resitive part of the antenna impedance is not very well equal to the chip impedance. This is partly due to high resistive losses in the tag as the thickness of the conductive sheet is much lower than the skin depth. A better resistive impedance match can be obtained by using conductive material with higher thickness. The reactive part of the impedance plotted in figure 3.14b along with the negative reactive impedance of the chip

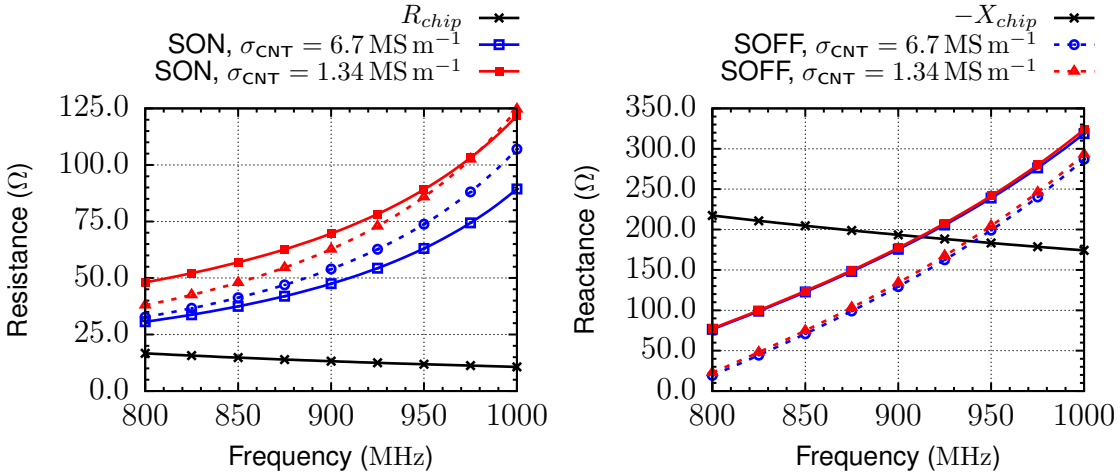

(a) Resistive part of Antenna Impedance. **(b)** Reactive part of Antenna Impedance.

Figure 3.14 *Simulation result showing the real and imaginary part of the antenna impedance of CNT sensor tag. Results with varying the conductivity of CNT material using SON and SOFF modes are shown. The chip impedance of RFID chip is also shown.*

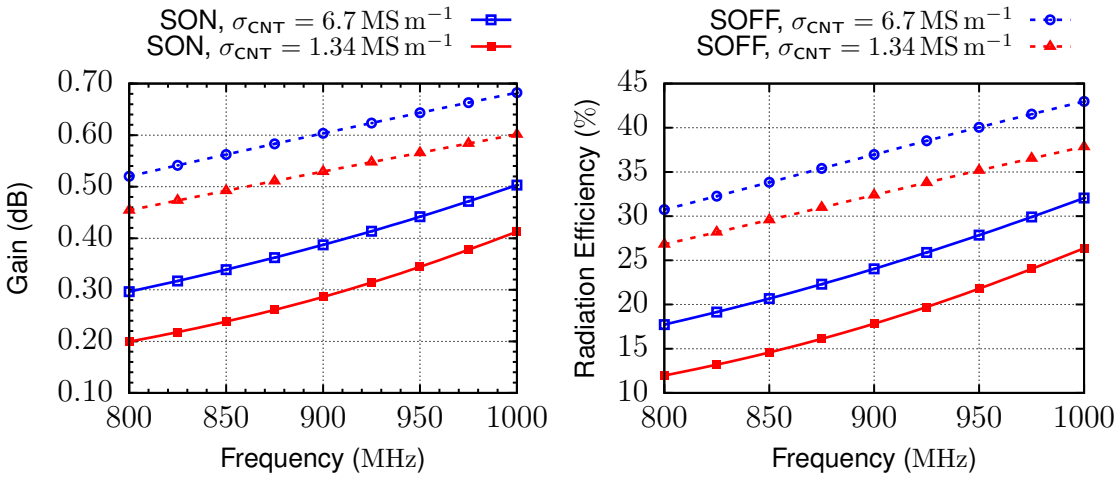

(a) Gain of CNT sensor tag. **(b)** Radiation Efficiency

Figure 3.15 *Simulation result showing gain and radiation efficiency of the CNT sensor tag. Gain is plotted along the z-axis with reference to the co-ordinate system shown in figure 3.10.*

shows the conjugate impedance match obtained. In SON mode with good and bad conductivity of CNT material, there is good conjugate impedance match at 915 MHz. SOFF mode creates an impedance mismatch.

The gain and radiation efficiency of the model simulated is shown in figure 3.15. It clearly shows the gain and radiation efficiency increasing quite considerably when the switch is turned off. With the conductivity of the CNT material lowered, radiation efficiency and gain drops in each mode of operation, SON and SOFF mode. The radiation efficiency with higher conductivity of CNT and in SON mode is quite low as 25 %. As expressed previously, this is due to the lower thickness of the printed Ag material, which is lower than its skin depth. Skin depth with conductivity of 1.23 MHz at 1 GHz frequency is 4.53 µm while the thickness of the tag modelled is 1 µm.

The plot of realized gain obtained from simulation is given previously in figure 3.11. This plot shows the impact of gain change or radiation efficiency change due to lowering the conductivity of the sensor part made of CNT material. This plot also shows the impact of the switch on the sensor. This should be read along with the impedance mismatch shown in figure 3.14b and the gain variation shown in figure 3.15a.

The computed read range using the expression shown in TABLE 3.3 is plotted

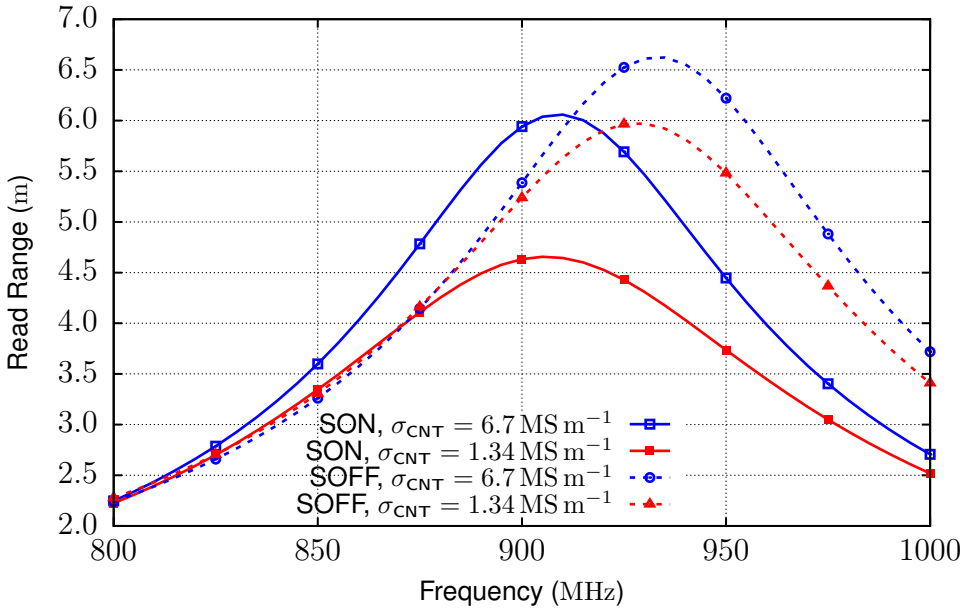

Figure 3.16 *Simulated read range values vs. frequency in SON and SOFF mode with different conductivity values for CNT. These measurements are along the z-axis with reference to the co-ordinate system shown in figure 3.10.*

in figure 3.16. The read range could be potentially increased by using thicker conductors as in [56] or using advanced techniques as in [59].

3.5.4 Sensing Paradigm

This section covers the possible method of making sensing measurement using a UHF RFID reader based on the design and simulation results obtained in the previous sections. It is evident from the previous section, that the change in the realized gain of the CNT sensor tag needs to be measured in order to sense the presence of CO_2 gas. Realized gain cannot be measured directly by the RFID reader device. Threshold power of the tag, explained in section 2.8.1.1, can be measured by the RFID reader by trying to find the minimum power at which the tag responds. Using the expression for threshold power, given in equation 2.33,

$$P_{chip} = \left(\frac{\lambda}{4\pi R}\right)^2 . G_{rTg} . G_{Rdr} . \eta_P . P_{Th},$$

the threshold power measurements made in SON mode and SOFF mode from the same tag can be expressed as,

$$G_{rTgSON}.P_{ThSON} = G_{rTgSOFF}.P_{ThSOFF}. \tag{3.1}$$

Here it is assumed that the reader performs measurements for SON and SOFF mode operation at the same time one after the other, by wirelessly controlling the switch. In addition, the measurements are done at the same distance between the reader and the tag, with the same frequency and with the same orientation. This condition implies the values, R, G_{Rdr}, η_P and λ become constants and hence get the above expression.

The above expression, when expressed in logarithmic scale becomes

$$P_{ThSONdB} - P_{ThSOFFdB} = -(G_{rTgSONdB} - G_{rTgSOFFdB}). \tag{3.2}$$

Hence any variation in realized gain difference between SON mode and SOFF mode operation can be measured by measuring the difference between threshold power of SON mode and SOFF mode operation. As previously shown in simulation results, realized gain of SOFF mode doesn't vary much in the desired frequencies of operation. Hence the difference in threshold power measurements is able to capture the variation in the realized gain of SON mode operation. In other words, the previous expression can be re-written as,

$$P_{ThSONdB}(\Psi) - P_{ThSOFFdB} = -(G_{rTgSONdB}(\Psi) - G_{rTgSOFFdB}). \tag{3.3}$$

where the variable quantities are shown to depend on the sensing parameter, Ψ, which shall represent CO_2 gas concentration.

It is important to note that the sensing measurement doesn't involve any absolute power measurement. It only depends on the relative difference between measurements in SON mode and SOFF mode operation. This implies that there is no need to have any precise calibrated setup involving the reader and the tag, to measure concentration of CO_2 gas in the environment.

However, there is a need to calibrate the variation of realized gain with relation to the changes in the concentration of CO_2 gas. This would help finding the inverse function to derive the sensed parameter, concentration of CO_2 gas or Ψ, from the

measurement made using equation 3.3. This is not considered in this work, but only the feasibility of CNT sensor to function as a detector by using a threshold.

3.6 Fabrication

This chapter discusses the fabrication process, step-by-step, of the RFID sensor tag. The materials used in the fabrication are described in section 3.2 above. Inkjet printing is the main tool used to create the prototype of sensor tags. Harima NPS-JL, Ag nanopaste and Polyink HC, CNT ink are inkjet printed on to substrate material, Kapton.

Harima NPS-JL Ag nanopaste is filtered through a 0.45 µm PTFE membrane syringe filter [38] while filling the printer cartridge. The printer cartridge is sonicated using the ultrasonic cleaning unit 'Elmasonic S 120' . Sonication is performed for 10 min at 35 °C. This helps removing bubbles inside the cartridge, and to bring the ink to room temperature, which is stored at 0 °C to 5 °C. The print cartridge is kept at room temperature for about an hour before printing.

The image of the pattern to be printed is prepared, as discussed in section 3.3.3. The pattern shown in figure 3.7a is inkjet printed on Kapton substrate using the parameters described in TABLE 3.1. The printed pattern is then thermally sintered at 150 °C for 60 min in an oven. Due to the issues discussed in section 3.3.2.3, there are unwanted silver traces near the edges of the printed pattern. These are cleaned using a hot soldering iron, to create clean substrate for printing the CNT ink pattern.

Polyink HC ink is filtered through a 0.45 µm PVDF membrane syringe filter [39] while filling the printer cartridge. The cartridge is then ready to print.

The CNT ink pattern shown in figure 3.7b is printed on the same substrate where the Ag ink is already printed earlier. Drop offset calibration (see section 3.3.2.5) is performed and the accurate reference point (see section 3.3.2.4) is chosen before printing. The parameters given in TABLE 3.1 is used during printing. The printed pattern is then sintered at 130 °C for 4 min in an oven. A multimeter, in the resistance measurement mode, is used to check any contact between Ag ink pattern (tag) and the CNT ink pattern (sensor). The edges of the Ag ink pattern are further cleaned using soldering iron, with a fine tip, to remove any contact between the tag and the sensor.

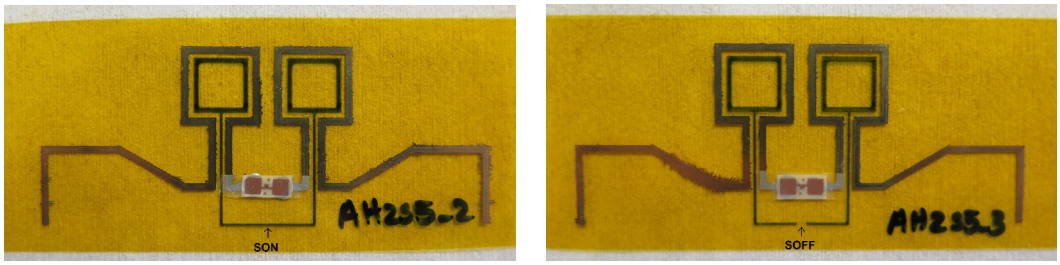

(a) Sensor On (SON) mode sample. **(b)** Sensor Off (SOFF) mode sample.

Figure 3.17 *The above pictures show two samples of the fabricated sensor tags. The sample on the right is modified to emulate the Sensor Off (SOFF) mode of operation. The location of the fictitious switch is marked in the picture.*

The RFID microchip, NXP's UCODE G2iL, is affixed to the terminals for the sensor tag using a conductive epoxy. The conductive epoxy is a two-part mixture which is mixed together and applied for bonding [11]. The bonding is cured at 75 °C for 15 min. The fictitious switch to create Sensor Off (SOFF) mode is created by using a dedicated sample, on which about 1 mm of CNT track is removed by scratching on the substrate with a sharp object. Two such fabricated samples kept on top of a white paper is shown in figure 3.17.

3.7 Measurements

The fabricated CNT sensor tags needs to be measured against an RFID reader in order to validate the sensing functionality. The measurement methodology is outlined by the sensing paradigm detailed in section 3.5.4. The motivation for the measurement setup can be found in [53]. The basic idea is to expose the CNT sensor tag to CO_2 gas and perform measurements using an UHF RFID tag reader, which is the 'Tagformance Lite' measurement unit from Voyantic (shown in figure 3.19c). Since the switch in the CNT sensor tag is not realized in this work, two samples, as shown in figure 3.17, are used for measurements. The two samples are measured separately, but under identical conditions, to obtain measurements under sensing (SON) mode and reference (SOFF) mode functionality. Using both samples, measurements were performed in two ways, which are explained below.

3.7.1 Online Measurements

Online or live measurements are measurements performed in a typical environment that is comparable to the actual application of the CNT senor tag. These measurements are taken while the CNT sensor tag is reacting with the CO_2 gas in its surroundings. The measurement setup used for this purpose is shown in figure 3.18. A lit candle is used to produce CO_2 gas. A hermetic box is used to confine the produced gas to a small space. The candle consumes oxygen inside the box while burning. The fire in the candle dies, after consuming all the oxygen inside the box, and at the same time produces more amount of CO_2 gas. The fabricated RFID sensor tag is glued inside the box at a marked location, as shown in figure 3.18b. Using Voyantic's wideband kit, an RFID reader antenna is mounted on a tripod and kept at about 1.5 m away from the CNT sensor tag. The reader antenna is kept at the same height as the tag inside the box and is horizontally aligned to match the polarization of the reader antenna and the tag. The tag is glued to a marked location inside the box. The Rx and Tx ports of the Voyantic Tagformance Lite UHF RFID measurement unit are connected to the antenna via a directional coupler and coaxial cable. The Tagformance measurement unit is connected to a PC (laptop shown in figure 3.18a) using an USB cable and the Tagformance measurement software running on the PC is able to make wireless measurements of the CNT sensor tag.

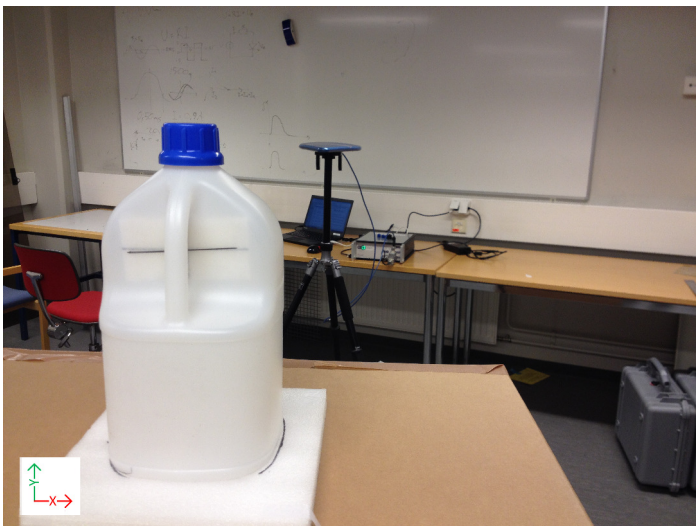

(a) Full view of the setup.

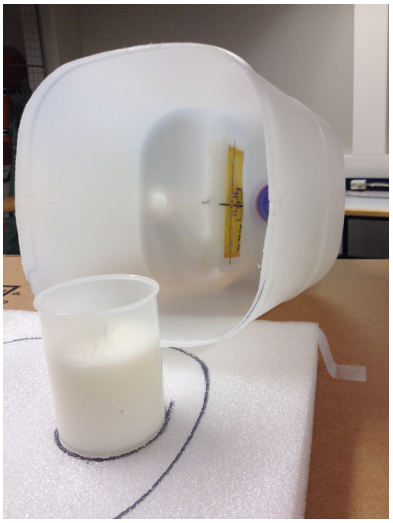

(b) Inside the box.

Figure 3.18 *The measurement setup used to validate* CO_2 *sensing functionality of fabricated CNT sensor tags. The RFID reader and the sensor are kept at about* 1.5 m *away. The sensor tag is glued inside the box as shown on right picture.*

Measurement setup named 'Threshold ' in the tagformance software is used for measurements. It measures the threshold power needed to activate the tag. Measurements were performed in the frequency range of 900 MHz to 930 MHz. The threshold power measurements are repeatedly performed to sense any change in its behavior during the experiment. As mentioned previously, the candle will die during the experiment after consuming all the oxygen inside the box. The candle is lit again after lifting the box momentarily and the measurements are continued. The candle is lit 4 times in total during this experiment.

During online measurements, the temperature inside the box also increases. Carbon nanotubes are known to change its conductivity due to variation of temperature as well [55]. Hence the measurements taken with this setup are showing the response not only to CO_2 gas, but also to temperature. In order to remove the impact of temperature in the measurements, offline measurements are used, which is described below.

3.7.2 Offline Measurements

The conductivity of CNT material is reduced in presence of CO_2 gas because of CO_2 gas molecules getting trapped in the CNT structure. The gas molecules will remain trapped even after its exposure to the gas. This causes a memory effect on the CNT sensor tag, such that the conductivity of the CNT material will remain reduced even after the experiment, described in the previous section, is completed. This memory effect of the CNT sensor tag offers an opportunity to make offline measurements inside an anechoic chamber. An anechoic chamber, shown in figure 3.19a, helps emulating the behaviour of an antenna kept in free space. This helps achieving results comparable to the results from simulation, which uses boundary conditions similar to free space.

Offline measurements are performed on the same sensor tags used for online measurements. They are kept at room temperature for some time to cool down. Since they were exposed to CO_2 gas, the CNT part of the sensor tag has lower conductivity. Thus the results obtained in this measurement are only in response to the CO_2 gas molecules trapped inside the CNT material. The CNT sensor tag is kept inside the anechoic chamber on a turn table at the centre of the chamber. The separation between the reader antenna and the tag, inside the chamber is roughly about 45 cm. This measurement setup is calibrated quite accurately, for the path loss involved in

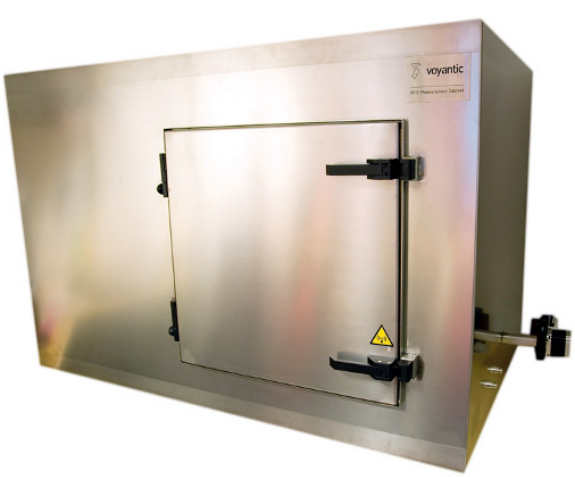

(a) Anacheoic Chamber.

(b) Reference tag

(c) Tagformance Lite.

Figure 3.19 *Offline measurement setup used to measure* CO_2 *sensing of fabricated CNT sensor tags, includes an Anechoic chamber and the tagformance lite UHF RFID measurement system. Pictures are not shown to scale.*

this wireless measurement setup, using the reference tag (shown in figure 3.19b) provided with tagformance lite measurement unit. Similar to offline measurements, 'Threshold ' measurements in the tagformance software are used for measurements. So tagformance measures the threshold power required to activate the tag. Since the path loss is calibrated already with a known reference tag, tagformance is able to compute additional results like, read range, power on tag forward, etc, using the measured threshold power values.

4. RESULTS AND ANALYSIS

In this chapter, the results of measurements conducted using the fabricated CNT sensor tags are discussed and analysed. The measurement methods are described in detail in the previous chapter (see section 3.7), and the principle behind these measurements are explained in section 3.5.4. Both online and offline measurements are performed along the z-axis, with respect to the co-ordinate system shown in figure 3.10. The measurement axis is consistent with the simulation measurement results shown in figure 3.11.

The threshold power measurements obtained during online measurements with the SON mode sample and the SOFF mode sample are shown in figure 4.1a and figure 4.1b respectively. During the experiment, the candle is lit 4 times and measurements at various instances of time are captured and shown here. The results show that the threshold power required to activate the SON mode CNT sensor tag is increasing from around 18 dBm to 22 dBm as the experiment proceeds. The SOF mode sample shows only a variation of around 0.5 dBm, at absolute threshold power level of around 18 dBm, during a similar experiment. These results prove the sens-

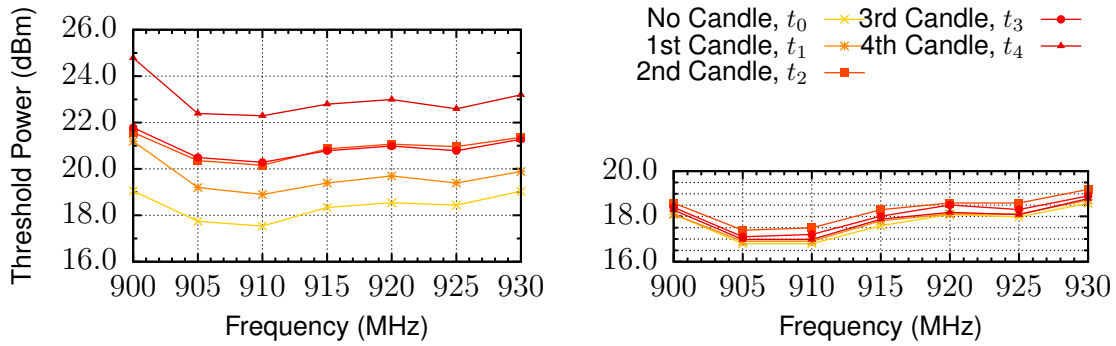

(a) Sensor On (SON) mode measurement. **(b)** Sensor Off (SOFF) mode measurement.

Figure 4.1 *Online measurement results showing variation of threshold power, required to activate the CNT sensor tag in SON and SOFF modes, at various instance of time during the tag's exposure to* CO_2 *gas and temperature under the candle.*

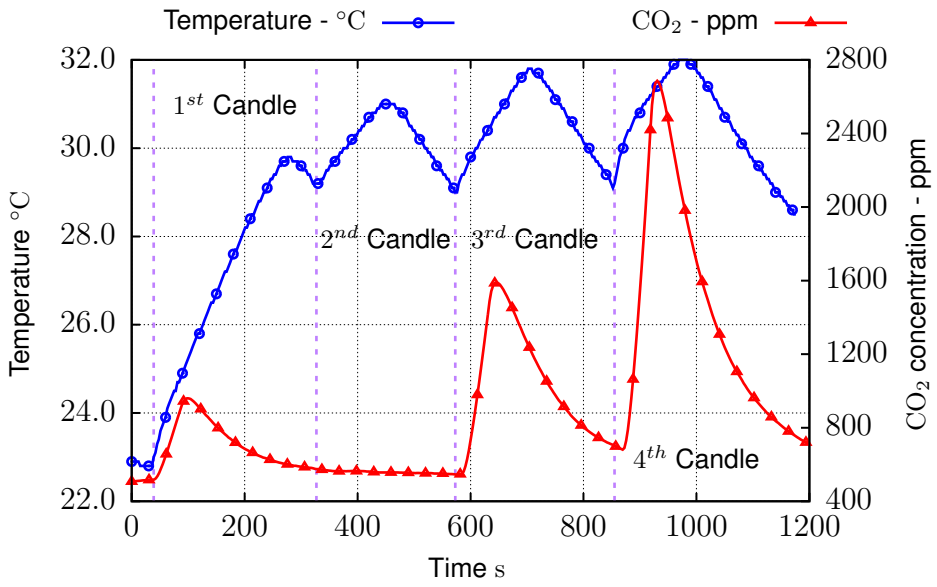

Figure 4.2 *Independent measurement of temperature and CO_2 gas concentration taken using the DeltaOhm datalogger HD37AB17D. These measurements are taken under identical conditions as the online measurement setup involving lighting of candle 4 times. Each candle period is marked in the plot.*

ing functionality of the CNT sensor tag, by the variation in realized gain during exposure to CO_2 gas and temperature. Figure 4.1b shows the functionality of its reference mode operation, by the lack of variation in realized gain with exposure to CO_2 gas and temperature.

Independent sensor measurements using DeltaOhm datalogger HD37AB17D [14] under similar experiment conditions are performed and results are shown in figure 4.2. It shows CO_2 gas concentrations increasing up to 2650 ppm in addition to about 10 °C increase in temperature during the experiment. It should be noted that the CO_2 gas concentrations achieved is quite random, in this experimental setup, as can be observed by the variation of the concentration during each candle burning period. Thus figure 4.2 gives only a rough idea of the temperature and CO_2 gas concentration levels at which the results shown in figure 4.1 are obtained.

Thus figure 4.1a and figure 4.2 shows a variation of up to 4 dB in threshold power to activate CNT sensor tag with exposure to around 30 °C temperature and 2500 ppm of CO_2 concentration. This shows good sensitivity of the sensor beyond measurement tolerances. Also, figure 4.1b shows negligible variation in threshold power under similar experiment conditions. These results prove functionality of CNT sensor tag with a good reference. But this measurement setup gives reaction of the sensor to

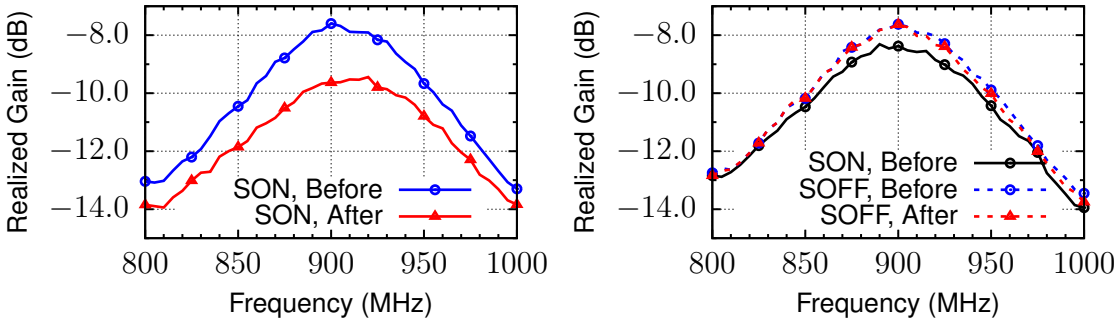

(a) Sensor On (SON) mode measurement. **(b)** Sensor Off (SOFF) mode measurement.

Figure 4.3 *Offline measurement results showing variation of realized gain, of CNT sensor tag in SON and SOFF modes, measured before and after the experiment for online measurements.*

both temperature and CO_2 gas.

As described in the previous chapter (section 3.7.2), offline measurements performed before and after the online measurement exercise helps isolating the performance of CNT sensor tag with exposure to CO_2 gas alone. Figure 4.3 shows the results from offline measurements. Measurements from the SON mode sample shown in figure 4.3a shows a variation of 2 dB in realized gain, which is comparable to the simulation measurement results shown in figure 3.11, obtained with 5 times reduction of conductivity of the CNT material. The measurements from the SOFF mode sample shown in figure 4.3b shows negligible variation in realized gain. Thus the offline measurement results show the capability of CNT sensor tag to function as CO_2 gas detector with a very good reference measurement using the switch in the sensor tag. Offline measurements also show that the CNT sensor tag has a memory effect, such that the sensor behaviour remains modified after exposure to CO_2 gas. In order to retrieve the CNT sensor tag to its initial state, it needs to be exposed to UV light for about 10 min. There is a hysteresis involved in this process, such that the CNT sensor tag doesn't fully return to its initial state, loosing some amount of sensitivity.

In figure 4.3b, the plot labelled 'SON, Before' shows the realized gain measured in SON mode, before the sample is converted to SOFF mode sample, by removing CNT track at the designated location of the switch. When the switch is turned off, an increase in realized gain can be observed. This is in line with the simulation results in figure 3.11. But the centre frequency of the tag doesn't shift compared

with the results from simulation. This phenomenon remains unexplained for now, and further study is required on this behaviour.

The read range of the CNT sensor tag decreases during sensing, as exposure to CO_2 reduces the gain of the tag as shown in figure 4.3a. It shows the realized gain reduces to about $-10\,\mathrm{dB}$ after the experiment. Realized gain of $-10\,\mathrm{dB}$ gives a read range of about 4m with 4W EIRP.

5. CONCLUSIONS

In this work, a novel passive UHF RFID based sensor tag with a built-in reference is realized for the purpose of wireless gas sensing. The RFID sensor tag is motivated by earlier work on the chipless sensor using inkjet printable CNT ink as shown in [55]. CNT ink material is used for purpose of CO_2 gas sensing, as it has the property of changing its conductivity in the presence of CO_2 gas. The most important aspect of this work is the switch used in the structure of the sensor tag, which allows two modes of operation, sensing mode and reference mode. An RFID reader device achieves sensing functionality by making threshold power measurements on the CNT sensor tag in both sensing mode and reference mode of operation. Measurement using the reference mode provides a baseline, capturing the impact of distance between the reader and the tag, and all other conditions in the wireless interrogation environment. Sensing or CO_2 gas detection is performed, by the reader, by taking the difference in threshold power values, of the CNT sensor tag, measured in the sensing mode and the reference mode.

CNT sensor tag is conceived, optimized and proven in the ANYSYS HFSS electromagnitic simulation environment. The designed sensor tag consists of a normal passive UHF RFID tag made of highly conductive material, and sensing functionality is included by placing CNT material close to the tag. The sensing part of the tag is the CNT material. Measurements in simulation environment showed good sensitivity for sensing based on assumed conductivity variation deduced from prior work [53]. Simulation results also showed good read range for the CNT sensor tag. Inkjet printing is used for the realization of the CNT sensor tag, on Kapton HN substrate material, using silver ink for highly conductive part of the sensor tag and CNT ink for the sensing part of the tag. The proposed switch in the sensor tag is not realized in this work. Instead, two separate samples were created to emulate the switch on (SON) mode or sensing mode, and switch off (SOFF) mode or reference mode of operation. These samples are subjected to exposure to CO_2 at similar experimental setup and measurements are taken using UHF RFID reader.

Results from various measurements performed shows about 2 dBm variation in threshold power required to activate the tag with sensing mode operation, after exposure to about 2500 ppm of CO_2 gas at about 30 °C. Measurements from SOFF mode samples show very little variation in threshold power under similar test conditions, proving the reference mode operation of the CNT sensor tag. Live measurements performed during the experiment show that the CNT sensor tag responds to temperature also. The sensitivity of the sensor due to temperature is quite high, showing up to 4 dBm variation. This shows potential of the sensor to function as temperature sensor also. The feasibility of using CNT material as temperature sensor was already shown in [54].

Study and measurements done in this work prove the feasibility of gas detection by placing CNT very close to the tag, instead of, on the tag. More importantly, the concept of using a switch in the sensor tag to provide reference measurement is proven. Several possibilities exist in the realization of the switch including, but not limited to, incorporating the switch within the RFID chip. These ideas will be explored in future work. CO2 and temperature sensing with calibrated measurements will also be studied in future work.

BIBLIOGRAPHY

[1] A. Adhur Kutty, T. Björninen, L. Sydänheimo, and L. Ukkonen, "A novel carbon nanotube loaded passive uhf rfid sensor tag with built-in reference for wireless gas sensing," 2016, in press, *International Microwave Symposium.*

[2] M. Akbari, L. Sydanheimo, J. Juuti, J. Vuorinen, and L. Ukkonen, "Characterization of graphene-based inkjet printed samples on flexible substrate for wireless sensing applications," in *RFID Technology and Applications Conference (RFID-TA), 2014 IEEE*, Sept 2014, pp. 135–139.

[3] K. Albrecht and L. Mcintyre, *Spychips: How Major Corporations and Government Plan to Track Your Every Move with RFID.* Pearson Education.

[4] *4NEC2: NEC based antenna modeler and optimizer*, Arie Voors. [Online]. Available: http://www.qsl.net/4nec2/

[5] O. Azucena, J. Kubby, D. Scarbrough, and C. Goldsmith, "Inkjet printing of passive microwave circuitry," in *Microwave Symposium Digest, 2008 IEEE MTT-S International*, June 2008, pp. 1075–1078.

[6] C. Balanis, *Antenna Theory: Analysis and Design*, 3rd ed. Wiley, 2012.

[7] R. Bhattacharyya, C. Floerkemeier, and S. Sarma, "Towards tag antenna based sensing - an rfid displacement sensor," in *RFID, 2009 IEEE International Conference on*, April 2009, pp. 95–102.

[8] T. Björninen, L. Sydänheimo, and L. Ukkonen, "Development and validation of an equivalent circuit model for uhf rfid ic based on wireless tag measurements," in *34th Annual Symposium of the Antenna Measurement Techniques Association*, October 2012, pp. 480–485.

[9] A. Bletsas, A. Dimitriou, and J. Sahalos, "Improving backscatter radio tag efficiency," *Microwave Theory and Techniques, IEEE Transactions on*, vol. 58, no. 6, pp. 1502–1509, June 2010.

[10] A. Boaventura, A. Collado, N. Carvalho, and A. Georgiadis, "Optimum behavior: Wireless power transmission system design through behavioral models and efficient synthesis techniques," *Microwave Magazine, IEEE*, vol. 14, no. 2, pp. 26–35, March 2013.

[11] *CircuitWorks Conductive Epoxy*, Chemtronics, August 2013, rev. K. [Online]. Available: https://www.chemtronics.com/descriptions/document/Cw2400tds.pdf

[12] B. Cook, T. Le, S. Palacios, A. Traille, and M. Tentzeris, "Only skin deep: Inkjet-printed zero-power sensors for large-scale rfid-integrated smart skins," *Microwave Magazine, IEEE*, vol. 14, no. 3, pp. 103–114, imsspecialissuemay 2013.

[13] B. Cook, R. Vyas, S. Kim, T. Thai, T. Le, A. Traille, H. Aubert, and M. Tentzeris, "Rfid-based sensors for zero-power autonomous wireless sensor networks," *Sensors Journal, IEEE*, vol. 14, no. 8, pp. 2419–2431, Aug 2014.

[14] *Datalogger RH - Temperature - CO - CO_2 HD37AB17D HD37B17D*, DeltaOhm, November 2009, rev.1.3. [Online]. Available: http://www.deltaohm.com/ver2012/index.php?main_page=product_info&cPath=1_13_29&products_id=16&zenid=hduo321jq61bn8d4icb9uq7hq7

[15] D. Dobkin, *The RF in RFID: Passive UHF RFID in Practice*, 2nd ed., ser. Communications engineering series. Elsevier Science, 2007. [Online]. Available: http://www.sciencedirect.com/science/book/9780750682091

[16] *Dimatix Materials Printer DMP-2800 Series User Manual*, Fujifilm, January 2010, rev. 04. [Online]. Available: https://www.seas.upenn.edu/~nanosop/documents/DMP2831_User_Manual.pdf

[17] *Dimatix Materials Printer DMP-2831*, Fujifilm, April 2013, rev. 02. [Online]. Available: http://www.fujifilmusa.com/support/ServiceSupportProduct.do?prodcat=879589

[18] *Gnu Image Manipulation Program*, GIMP. [Online]. Available: https://www.gimp.org/

[19] R. Goncalves, S. Rima, R. Magueta, P. Pinho, A. Collado, A. Georgiadis, J. Hester, N. Borges Carvalho, and M. Tentzeris, "Rfid-based wireless passive sensors utilizing cork materials," *Sensors Journal, IEEE*, vol. 15, no. 12, pp. 7242–7251, Dec 2015.

[20] B. Guru and H. Hiziroglu, *Electromagnetic Field Theory Fundamentals*, 2nd ed. Cambridge University Press, 2004.

[21] *NANOPASTE series brochure*, Harima Chemicals Group. [Online]. Available: https://www.harima.co.jp/en/products/electronics/pdf/brochure16e_23.pdf

[22] R. Harrington, "Electromagnetic scattering by antennas," *Antennas and Propagation, IEEE Transactions on*, vol. 11, no. 5, pp. 595–596, Sep 1963.

[23] R. F. Harrington, "Theory of loaded scatterers," *Electrical Engineers, Proceedings of the Institution of*, vol. 111, no. 4, pp. 617–623, April 1964.

[24] M. Hasani, A. Vena, L. Sydanheimo, L. Ukkonen, and M. Tentzeris, "Implementation of a dual-interrogation-mode embroidered rfid-enabled strain sensor," *Antennas and Wireless Propagation Letters, IEEE*, vol. 12, pp. 1272–1275, 2013.

[25] S. Iijima, "Helical microtubules of graphitic carbon," *Nature*, vol. 354, pp. 56–58, 1991. [Online]. Available: http://dx.doi.org/10.1038/354056a0

[26] K. Koski, E. Koski, J. Virtanen, T. Björninen, L. Sydänheimo, L. Ukkonen, and A. Z. Elsherbeni, "Inkjet-printed passive uhf rfid tags: review and performance evaluation," *The International Journal of Advanced Manufacturing Technology*, vol. 62, no. 1, pp. 167–182, 2011. [Online]. Available: http://dx.doi.org/10.1007/s00170-011-3782-8

[27] J. Landt, "The history of rfid," *Potentials, IEEE*, vol. 24, no. 4, pp. 8–11, Oct 2005.

[28] G. Marrocco, "The art of uhf rfid antenna design: impedance-matching and size-reduction techniques," *Antennas and Propagation Magazine, IEEE*, vol. 50, no. 1, pp. 66–79, Feb 2008.

[29] G. Marrocco and F. Amato, "Self-sensing passive rfid: From theory to tag design and experimentation," in *Microwave Conference, 2009. EuMC 2009. European*, Sept 2009, pp. 001–004.

[30] G. Marrocco , "Pervasive electromagnetics: sensing paradigms by passive rfid technology," *Wireless Communications, IEEE*, vol. 17, no. 6, pp. 10–17, December 2010.

[31] S. Merilampi, T. Bjorninen, A. Vuorimaki, L. Ukkonen, P. Ruuskanen, and L. Sydanheimo, "The effect of conductive ink layer thickness on the functioning of printed uhf rfid antennas," *Proceedings of the IEEE*, vol. 98, no. 9, pp. 1610–1619, Sept 2010.

[32] K. Mittal, *Contact Angle, Wettability and Adhesion*. Taylor & Francis, 2003, no. nid. 3. [Online]. Available: https://books.google.fi/books?id=lTlRAAAAMAAJ

[33] *ACE Translator 3000*, Numerical Innovations. [Online]. Available: http://www.numericalinnovations.com/collections/ace-translator-3000

[34] *SL3S1203/1213: UCODE G2iL and G2iL+*, NXP Semiconductors, March 2014, rev. 4.4. [Online]. Available: http://www.nxp.com/products/identification-and-security/smart-label-and-tag-ics/ucode/ucode-g2il-and-g2il-plus:SL3S1203_1213

[35] C. Occhiuzzi, S. Caizzone, and G. Marrocco, "Passive uhf rfid antennas for sensing applications: Principles, methods, and classifcations," *Antennas and Propagation Magazine, IEEE*, vol. 55, no. 6, pp. 14–34, Dec 2013.

[36] C. Occhiuzzi, A. Rida, G. Marrocco, and M. Tentzeris, "Rfid passive gas sensor integrating carbon nanotubes," *Microwave Theory and Techniques, IEEE Transactions on*, vol. 59, no. 10, pp. 2674–2684, Oct 2011.

[37] H. A. of German Research Centres, "Inkjet printing process for kesterite solar cells," *Phy.org*, 2015. [Online]. Available: http://phys.org/news/2015-05-inkjet-kesterite-solar-cells.html

[38] *Acrodisc® Syringe Filters with PTFE Membrane*, Pall Corporation. [Online]. Available: http://www.pall.com/main/laboratory/product.page?id=19988

[39] *Acrodisc® Syringe Filters with PVDF Membrane*, Pall Corporation. [Online]. Available: http://www.pall.com/main/laboratory/product.page?id=19989

[40] *Poly-Ink HC Datasheet*, Poly-Ink, dataSheet-V6. [Online]. Available: http://poly-ink.fr/index.php/en/our-products/poly-ink-hc.html

[41] D. Pozar, *Microwave Engineering, 4th Edition*, 4th ed. Wiley, 2011.

[42] K. Rao, P. Nikitin, and S. Lam, "Antenna design for uhf rfid tags: a review and a practical application," *Antennas and Propagation, IEEE Transactions on*, vol. 53, no. 12, pp. 3870–3876, Dec 2005.

[43] K. Rao, P. Nikitin, and S. Lam , "Impedance matching concepts in rfid transponder design," in *Automatic Identification Advanced Technologies, 2005. Fourth IEEE Workshop on*, Oct 2005, pp. 39–42.

[44] M. Reich and C. Bauer-Reich, "Uhf rfid impedance matching: When is a t-match not a t-match?" in *RFID (IEEE RFID), 2014 IEEE International Conference on*, April 2014, pp. 23–30.

[45] A. Rida, L. Yang, R. Vyas, and M. Tentzeris, "Conductive inkjet-printed antennas on flexible low-cost paper-based substrates for rfid and wsn applications," *Antennas and Propagation Magazine, IEEE*, vol. 51, no. 3, pp. 13–23, June 2009.

[46] M. Rizwan, A. Adhur Kutty, M. Kgwadi, T. D. Drysdale, L. Ukkonen, and J. Virkki, "Comparitive study of inkjet and thermal printing for fabrication of passive uhf rfid tags," 2016, in press, *10th European Conference on Antennas and Propagation*.

[47] M. Rizwan , A. Adhur Kutty, M. Kgwadi, T. D. Drysdale, L. Ukkonen, and J. Virkki, "Reliability study of flexible inkjet- and thermal- printed rfid antennas in high humidity conditions," 2016, in press, *10th European Conference on Antennas and Propagation*.

[48] J. Siden, M. Fein, A. Koptyug, and H. Nilsson, "Printed antennas with variable conductive ink layer thickness," *Microwaves, Antennas Propagation, IET*, vol. 1, no. 2, pp. 401–407, April 2007.

[49] H. Stockman, "Communication by means of reflected power," *Proceedings of the IRE*, vol. 36, no. 10, pp. 1196–1204, Oct 1948.

[50] W. Stutzman and G. Thiele, *Antenna Theory and Design*, 3rd ed. Wiley, 2012.

[51] V. Subramanian, J. Frechet, P. Chang, D. Huang, J. Lee, S. Molesa, A. Murphy, D. Redinger, and S. Volkman, "Progress toward development of all-printed rfid tags: Materials, processes, and devices," *Proceedings of the IEEE*, vol. 93, no. 7, pp. 1330–1338, July 2005.

[52] A. Toccafondi and P. Braconi, "Compact load-bars meander line antenna for uhf rfid transponder," in *Antennas and Propagation, 2006. EuCAP 2006. First European Conference on*, Nov 2006, pp. 1–4.

[53] A. Vena, L. Sydanheimo, M. Tentzeris, and L. Ukkonen, "A novel inkjet printed carbon nanotube-based chipless rfid sensor for gas detection," in *Microwave Conference (EuMC), 2013 European*, Oct 2013, pp. 9–12.

[54] A. Vena, L. Sydanheimo, L. Ukkonen, and M. Tentzeris, "A fully inkjet-printed chipless rfid gas and temperature sensor on paper," in *RFID Technology and Applications Conference (RFID-TA), 2014 IEEE*, Sept 2014, pp. 115–120.

[55] A. Vena, L. Sydänheimo, M. Tentzeris, and L. Ukkonen, "A fully inkjet-printed wireless and chipless sensor for co2 and temperature detection," *Sensors Journal, IEEE*, vol. 15, no. 1, pp. 89–99, Jan 2015.

[56] J. Virtanen, T. Bjorninen, L. Ukkonen, K. Kaija, T. Joutsenoja, L. Sydanheimo, and A. Elsherbeni, "The effect of conductor thickness in passive inkjet printed rfid tags," in *Antennas and Propagation Society International Symposium (APSURSI), 2010 IEEE*, July 2010, pp. 1–4.

[57] J. Virtanen, L. Ukkonen, T. Bjorninen, A. Elsherbeni, and L. Syda?nheimo, "Inkjet-printed humidity sensor for passive uhf rfid systems," *Instrumentation and Measurement, IEEE Transactions on*, vol. 60, no. 8, pp. 2768–2777, Aug 2011.

[58] J. Virtanen, L. Ukkonen, T. Bjorninen, L. Sydanheimo, and A. Elsherbeni, "Temperature sensor tag for passive uhf rfid systems," in *Sensors Applications Symposium (SAS), 2011 IEEE*, Feb 2011, pp. 312–317.

[59] J. Virtanen, J. Virkki, A. Z. Elsherbeni, L. Sydänheimo, and L. Ukkonen, "A selective ink deposition method for the cost-performance optimization of inkjet-printed uhf rfid tag antennas," *International Journal of Antennas and Propagation*, vol. 2012, 2012. [Online]. Available: http://dx.doi.org/10.1155/2012/801014

[60] J. Virtanen, F. Yang, L. Ukkonen, A. Elsherbeni, A. Babar, and L. Sydänheimo, "Dual port temperature sensor tag for passive uhf rfid systems," *Sensor Review*, vol. 34, no. 2, pp. 154–169, 2014. [Online]. Available: http://dx.doi.org/10.1108/SR-12-2011-681

[61] V. Vishwakarma, S. S. Samal, N. Manoharan, and C. F. Nanoscience, "Manoharan n: Safety and risk associated with nanoparticles- a review," *J Mineral and Mat Char Eng*, pp. 9–455.

[62] A. Walton, *Microelectronic test structures*. Kluwer, 1998. [Online]. Available: http://citeseerx.ist.psu.edu/viewdoc/download?doi=10.1.1.28.1685&rep=rep1&type=pdf

[63] Y. Wang and J. T. W. Yeow, "A review of carbon nanotubes-based gas sensors," *Journal of Sensors*, vol. 2009, no. 493904, 2009. [Online]. Available: http://dx.doi.org/10.1155/2009/493904

[64] R. Want, "Enabling ubiquitous sensing with rfid," *Computer*, vol. 37, no. 4, pp. 84–86, April 2004.

[65] R. Want , "An introduction to rfid technology," *Pervasive Computing, IEEE*, vol. 5, no. 1, pp. 25–33, Jan 2006.

[66] R. Wolf and A. C. Sparavigna, "Role of plasma surface treatments on wetting and adhesion," *Engineering*, vol. 2, no. 6, pp. 397–402, 2010. [Online]. Available: http://dx.doi.org/10.4236/eng.2010.26052

[67] L. Yang, R. Zhang, D. Staiculescu, C. Wong, and M. Tentzeris, "A novel conformal rfid-enabled module utilizing inkjet-printed antennas and carbon nanotubes for gas-detection applications," *Antennas and Wireless Propagation Letters, IEEE*, vol. 8, pp. 653–656, 2009.